Statistical modelling of cracking in large concrete structures under Thermo-Hydro-Mechanical loads: Application to Nuclear Containment Buildings. Part 2: Sensitivity analysis

David Bouhjiti, Maria Blasone, Julien Baroth, Frédéric Dufour, Benoît Masson, Sylvie Michel-Ponnelle

Statistical modelling of cracking in large concrete structures under Thermo-Hydro-Mechanical loads: Application to Nuclear Containment Buildings. Part 2: Sensitivity analysis

D.E.-M. Bouhjiti[a,b,*], M.C. Blasone[a,b], J. Baroth[a,*], F. Dufour[a,c], B. Masson[d], S. Michel-Ponnelle[e]

[a] Univ. Grenoble Alpes, CNRS, Grenoble INP[1], 3SR, F-38000, Grenoble, France
[b] Grenoble INP Partnership Foundation – Industrial chair PERENITI, Grenoble, France
[c] PERENITI chairholder (EDF SEPTEN/DTG/CIH), France
[d] Electricité De France (EDF-SEPTEN), Lyon, France
[e] Electricité De France (EDF-R&D), Paris, France

As demonstrated in Part I of this contribution, the precise and full prediction of the cracking patterns and concrete's global behaviour in ageing structures is a complex task. Though the suggested modelling strategy allows the prediction of the main cracking patterns, its drawbacks are mainly related to (a) the use of the so-called Statistical Size Effect Law requiring various random field realizations (more than 30) and (b) the iden-tification of a consequent number of Thermo-Hydro-Mechanical parameters (more than 50) which variations may also affect the computed cracking patterns and ageing behaviour. In part II of this contribution, the aim is to evaluate the effect of such uncertainty-related variations on concrete's early age and long term behaviours (in comparison with the effect of the intrinsic spatial variation of mechanical properties in part I). With that regard, a 1st order sensitivity analysis to the various input's variation is performed using the OFAT method. Throughout the study, the robustness (model's convergence) and predictiveness (physical representativeness of numerical results) of the suggested model in Part I are evaluated within the identified inputs' variation domains. The obtained results, in terms of the 1st order global sensitivity indexes, provide a subjectively quantitative and objectively qualitative ordering of the most influential parameters within the model's associated physical hy-potheses. In particular, the obtained results show (a) the relevance of the Gaussian function to describe the spatial correlation of the Young's modulus property (b) the dependence of early age behaviour on, both, the spatial scattering of the mechanical properties and the maturity process; but mostly, on the structural size effect assessment (c) the main dependence of long term behaviour on the drying history and applied prestressing loads and (d) the importance of uncertainties propagation through the Thermo-Hydro-Mechanical calculations and through the operational lifespan of ageing concrete structures.

1. Introduction

The uncertainties related to a given quantity are the consequence of either the intrinsic variations of its measurement system composed by, both, the material and studied phenomena or of an induced error of the measuring method (Ditlevsen and Madsen, 1996). In the case of concrete cracking, the sources of uncertainties are numerous and can be classified into two groups (Baroth et al., 2011):

– The first group encloses the internal sources of uncertainties related to the internal state of the structure. It has to do with the concrete's properties (more than 50 parameters are needed for a full THM calculation covering both early age and delayed behaviour (Bouhjiti et al., 2018) – Fig. 1), the structural design (geometry and rebars disposals for example – Fig. 2) and the internal interactions between different structural parts (restraining effects for instance).
– The second group is related to external sources of uncertainties; mainly, the variation of the THM boundary conditions. Some of those uncertainties are inevitable and cannot be reduced or deleted. Yet, they are quantifiable (such as the CoV of the mechanical

* Corresponding authors at: Grenoble INP Partnership Foundation – Industrial chair PERENITI, Grenoble, France.
E-mail addresses: david.bouhjiti@3sr-grenoble.fr (D.E.-M. Bouhjiti), maria.blasone@3sr-grenoble.fr (M.C. Blasone), julien.baroth@3sr-grenoble.fr (J. Baroth), frederic.dufour@3sr-grenoble.fr (F. Dufour), benoit.masson@edf.fr (B. Masson), sylvie.michel-ponnelle@edf.fr (S. Michel-Ponnelle).
[1] Institute of Engineering Univ. Grenoble Alpes.

Nomenclature

CoV	coefficient of variation
DOE	design of experiments
FE	finite elements
GSA	global sensitivity analysis
NCB	Nuclear Containment Buildings
OFAT	one-factor-at-a-time
OP	operational phase
POP	pre-operational phase
RF	random fields
RH	relative humidity
RSV	representative structural volume
SSEL	statistical size effect law
THM	Thermo-Hydro-Mechanical
VeRCoRs	French acronym for '' VErification Réaliste du COnfinement des RéacteurS '' meaning '' Realistic assessment of the nuclear reactors' tightness ''

properties). Other epistemic uncertainties can be reduced thanks to a better understating of the phenomena and an improvement of the measurement precision and quality (for instance the parameters related to the use of RF and to the modelling of THM properties' spatial randomness). And, finally, other ontological uncertainties which are rather related to the human nature of continuous learning process and skills' improvement; for example, the construction quality on the field.

In front of such diverse sources of uncertainties, and considering the consequent number of inputs and hefty computational time (from 4 h to 2 days for a full THM analysis at the RSV scale – Figs. 1 and 2), the decision making process with regards to cracking control, maintenance and repair operations remains quite complex. Therefore, and for the previously presented modelling strategy (Bouhjiti et al., 2018), the model's sensitivity to such uncertainty-induced variations is a key question with regards to its robustness (model's convergence) and predictiveness (model's physical representativeness) in terms of qualitative and quantitative description of cracking. Moreover, for the sake of applicability and practicality of use, the identification of the model's most influential parameters is required. On the one hand, this would gear experimental work towards the identification of critical parameters and the understanding of key phenomena. On the other hand, it would introduce – in the case of non-influential parameters – additional hypotheses aiming at facilitating the model's usage and eventually reducing its required inputs' number for the considered structural volumes and loads. Indeed, such simplifications remain strongly dependent on the considered structure and its environment; they can only be performed if the model's ability to accurately describe the foreseen THM behaviour is not altered.

Existing contributions with that regard remain partial focusing on one of the THM calculation steps without evaluating the uncertainties propagation through the THM steps and throughout the operational lifespan of structures. Moreover, they are limited to either the early age behaviour until the thermo-hydration phase ends (Briffaut et al., 2012; Xian et al., 2014) or the long term behaviour where early age effects are overlooked (Defraeye et al., 2013; Trabelsi et al., 2012; de Larrard et al., 2010):

- Early age sensitivity analysis: In (Briffaut et al., 2012; Xian et al., 2014), a 1st order sensitivity analysis is performed to study the effects of concrete's thermal behaviour during hydration on its cracking risk based on a global stress analysis. By using the ratio of the developed stress (within a viscoelastic framework) to the tensile strength as an index, it is shown in Briffaut et al. (2012) that the self-induced cracking risk of a 1.2 m thick wall is up to 30% higher when the effects of hydration and temperature on the concrete's thermal capacity are not considered. This, however, should be viewed as a relative increase of the developed tensile stresses in the concrete volume and not as a given probability of cracking. Indeed, the

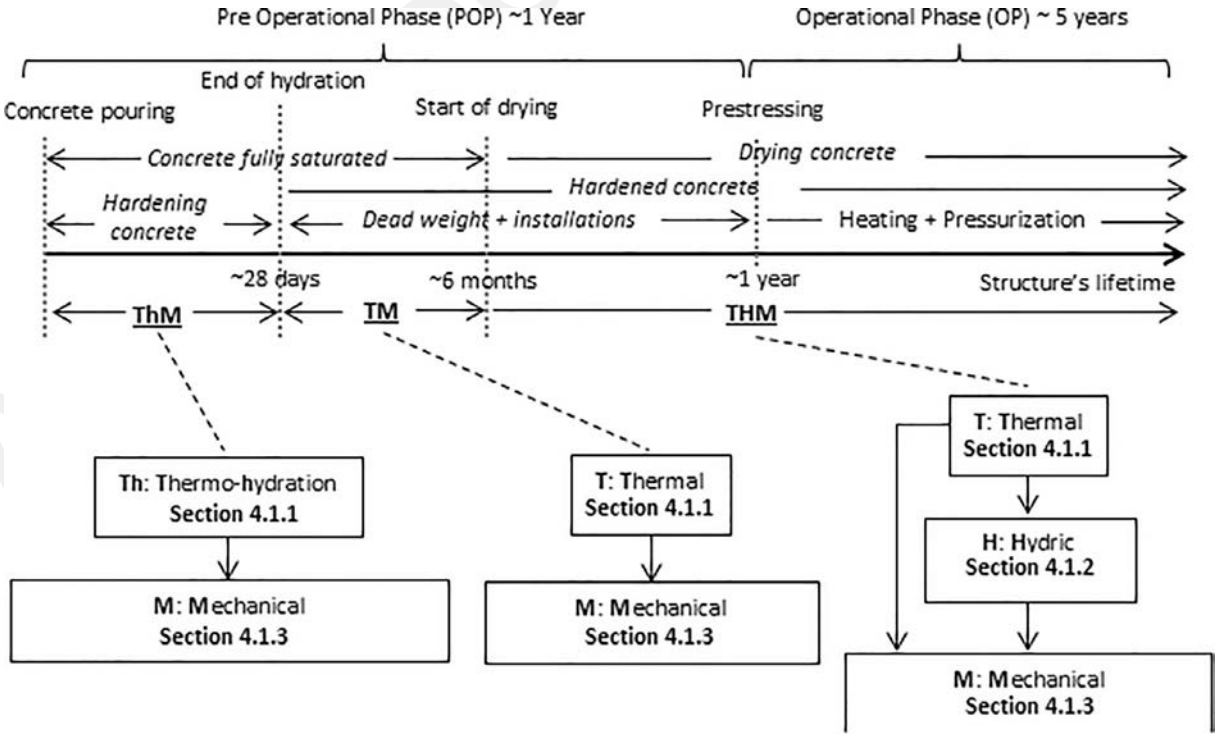

Fig. 1. Overall view of the THM modelling steps applied to the 1:3 scale VeRCoRs mock-up in Fig. 2 (Bouhjiti et al., 2018).

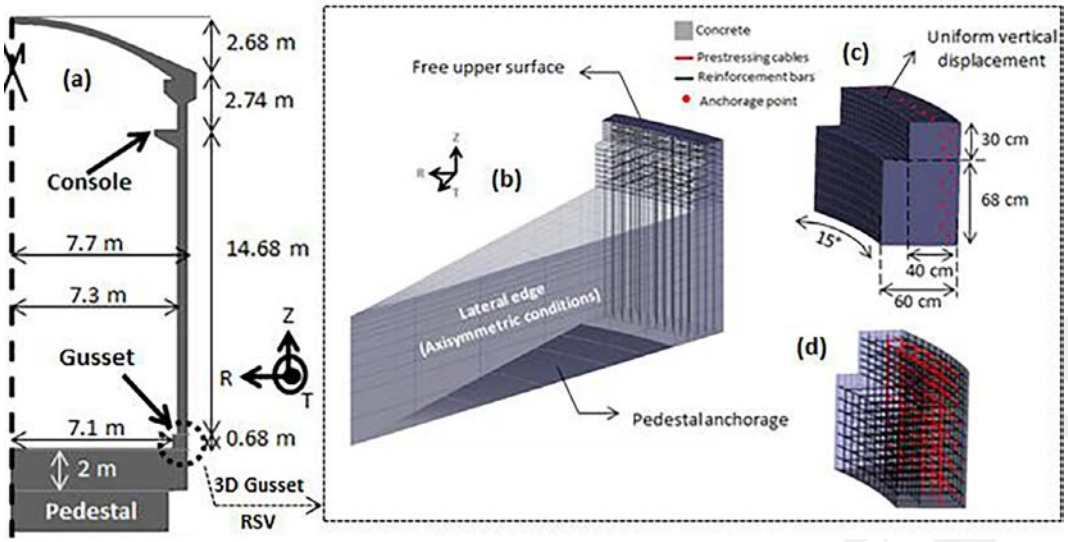

Fig. 2. VeRCoRs mock-up (Nuclear containment building – scale 1:3) (a) 2D-AXIS view of the inner wall (b) FE model of the gusset and the base slab RSV at early age (c) FE model of the gusset and anchorage nodes for the operational phase (d) 1D finite elements of rebars and prestressing cables (Quadratic elements for the concrete and linear elements for steel) (Bouhjiti et al., 2018).

obtained stresses in that analysis remained 50% less than the developed tensile strength of concrete which means that, practically, and in the absence of any considered size effects, whether the thermal and hydration effects have been considered or not, the considered wall would not have developed any cracks. In (Xian et al., 2014), where analysis is also viscoelastic, it is demonstrated numerically that the curing and ambient temperatures are the most important aspects that affect concrete cracking at early age. In another contribution (Briffaut et al., 2011), a damage-based viscoelastic model has been considered in order to evaluate the contribution of creep at early age to damage. The concrete's thermal properties have been considered constant and the application covered a 2D axisymmetric 1.8 m and 1.2 m thick walls. It is shown that concrete damage might be considerably overestimated when its early age creep is overlooked. It is worth underlining that in all previous studies (Briffaut et al., 2011, 2012; Xian et al., 2014), the explicit modelling of concrete cracking patterns is lacked, no comparison between the effects of thermo-hydration and of viscoelastic behaviour on cracking is performed and size effects are not considered. Therefore, a quantitative analysis of cracking is needed to accurately designate the most influential parameters considering a random full 3D damage-based viscoelastic analysis as shown in Part I (Bouhjiti et al., 2018).

- Long term sensitivity analysis: For large structures, previous studies have covered the effects of concrete properties' spatial scattering (hydric properties in Defraeye et al. (2013), Trabelsi et al. (2012) and mechanical properties in Bouhjiti et al. (2018), de Larrard et al. (2010)) on its observed behaviour and durability. Despite the underlined importance of such variability on the concrete's response, a clear ordering of the various THM inputs with regards to their importance is lacked. Based on a viscoelastic analysis, it is concluded in Berveiller et al. (2007a) that the water diffusivity factors and the desorption curve parameters are the most influential with regards to concrete drying and, within the used coefficients of variation, have insignificant effect on the concrete's viscoelastic response. It is worth noting, however, that the inputs' distribution were considered arbitrarily uniform (Berveiller et al., 2007a) and the considered lower and upper bonds of the desorption curve were not physically realistic. Besides, despite the absence of early age damage, questions related to the effects of viscoelastic parameters variation on the ageing of concrete and its long term cracking risk remain unanswered.

Eventually, a more global sensitivity analysis covering both early-age and long term phases and also aiming at the quantification of the cracking risk is still required. Once performed, the obtained results shall allow an enhanced identification of the most influential parameters that one might retain for higher order sensitivity analysis, uncertainty propagation and probabilistic analyses (Berveiller et al., 2007b).

Following the 1st part, this contribution (Part II) aims essentially at (a) providing a quantitative sensitivity analysis of concrete cracking under simultaneous THM loads accounting for both statistical and energetic size effects and (b) performing a global and selective uncertainty propagation throughout the whole THM chain retaining only the most influential parameters and most significant modelling hypotheses (in the case of the gusset RSV Fig. 2). To serve this purpose, and given the required computational time for a full THM simulation (~4 h to ~2 days) and number of inputs to characterize (~50 parameters), the OFAT method (Saltelli et al., 2018), Cotter (1979) is used to achieve a 1st order sensitivity analysis of the THM model's dependence on the various inputs variation. It consists of computing the THM model for the lower and upper limits of each input (whereas the remaining inputs are equal to their mean values). By definition, the number of model calls is minimal and equal to two times the number of model's inputs (in addition to the reference analysis where all inputs have a mean value). The lower and upper bounds of each input (defining the variation domain) are identified based on experimental results when available; otherwise expert judgments are retained to illustrate the high uncertainty of some model's parameters. Compared to other DOE methods such as the Fractional Factorial sampling, Latin Hypercube Sampling, Stratified Sampling or (Quasi-) Random Sampling, the OFAT method remains considerably less time consuming as no correlations between the various inputs is considered. However, and as a second step, one might perform higher order sensitivity analyses once the most influential parameters are defined thanks to the 1st order OFAT method. Priority, in that sense, should be granted to correlation analysis of the reduced list of important inputs and their associated physical phenomena (not covered in this contribution). Consequently, this contribution is threefold:

– The first part highlights the range of data scattering observed on site

in the case of the VeRCoRs gusset (Corbin and Garcia, 2015). The analysis of strain variations leads to the realistic assessment of in situ thermal and mechanical behaviour variation; especially the structural restraining effects affecting the gusset's response under prestressing and pressurization loads. Within this part, the retained model's ability to describe structural (global and local) effects and its limitations are also recalled in comparison with realistic observations.

- The second part describes the general 1st order sensitivity analysis strategy along with the used global and partial 1st order sensitivity indexes performed per every THM step. After briefly recalling the descriptive equations for each THM step, uncertainties propagation from the T to the M calculations is achieved. Only the most important parameters are retained per step to limit the number of simulations and focus on most influential inputs with regards to cracking. An inverse analysis is also performed in an attempt to define the variation domains of each THM parameter based on in-situ observations.
- The third and final part discusses the associated domain of variation of each input as well as the model's response to these variations in the case of the VeRCoRs gusset RSV (Bouhjiti et al., 2018). Eventually, a reduced list of parameters affecting concrete cracking is provided for better understanding of concrete cracking, better monitoring and better modelling of concrete behaviour in large structures such as NCBs.

2. In-situ data scattering of the VeRCoRs gusset

At the gusset level there are 6 angular positions at which sensors have been placed as shown in Fig. 3 (Corbin and Garcia, 2015).

The 'F' sensors are the ones close to the base slab at an elevation of −0.95 m and the 'G' sensors are located at an elevation of −0.25 m. Sensors with even numbers are located on the extrados side and those with odd numbers are on the intrados, both, at a cover distance of 5 cm. Two classes of sensors can be distinguished: the first one is for sensors that may undergo a structural effect due to their presence in the vicinity of the mock-up's ribs $\{F_X,G_X/\ X\in [3,8]\}$ and others in a 'standard' zone of the gusset where the ribs' effect is the least $\{F_X,G_X/\ X\in [1,2]\cup 9,12]\}$. Four additional sensors {F102,G102,F304,G304} are placed in the core of concrete between F_1 and F_2, G_1 and G_2, F_3 and F_4 and G_3 and G_4 respectively. The observed CoV for our variables of interest (temperature, strain values and cracking patterns) are summed up in Table 1.

2.1. Global behaviour during the pre-operational phase (POP)

The variation of temperature during hydration (Fig. 4) can be caused by the variation of the applied thermal boundaries and by the intrinsic variation of the thermal properties themselves. For the peak temperature in the VeRCoRs gusset, a CoV of 6% is observed describing a variation of ± 4°C for, both, F and G sensors. The temperature profile over time is also different from a sensor to another due to the non-uniform thermal boundary conditions around the gusset. Once the hydration ends, the variation of the temperature profiles is limited mostly to ± 1°C which is the sensor's precision.

As for strain measurements, the sources of uncertainties are more numerous. In addition to the mechanical boundaries between the gusset and the base slab and the random spatial distribution of the mechanical properties, one can enumerate the inclination of the gauges, the development of nearby cracks and the dependence on the thermal behaviour itself (propagation of uncertainties from Th to M step in Fig. 1). These are crucial aspects to be considered while assessing the precision of the performed measurements.

The variation of vertical and tangential strains is more important compared to the one of temperature. In the vertical direction (Fig. 5), a CoV of 25% is observed for the peak strain at early age in the case of F sensors (and of 12% in the case of G sensors). Tangential and vertical train components are less important nearby the restraining joint area (level −0.95 m) – same tendencies are obtained numerically (Bouhjiti et al., 2018) – but more scattered compared to elevated sensors (level −0.25 m). In the tangential direction (Fig. 5) and sufficiently away from macrocracks (Sensors G12, F9 and F10 discarded), the observed CoV is of the same order of magnitude for both levels (around 30%) though the strains are naturally more restrained in the vicinity of the base slab (numerical simulations show the same tendency (Bouhjiti et al., 2018). In the case of G sensors, the extrados side seems to develop more compressive tangential and vertical strains compared to the intrados. At the lower level (−0.95 m), the behaviour is reversed in the vertical direction; meaning that the intrados seems to be more

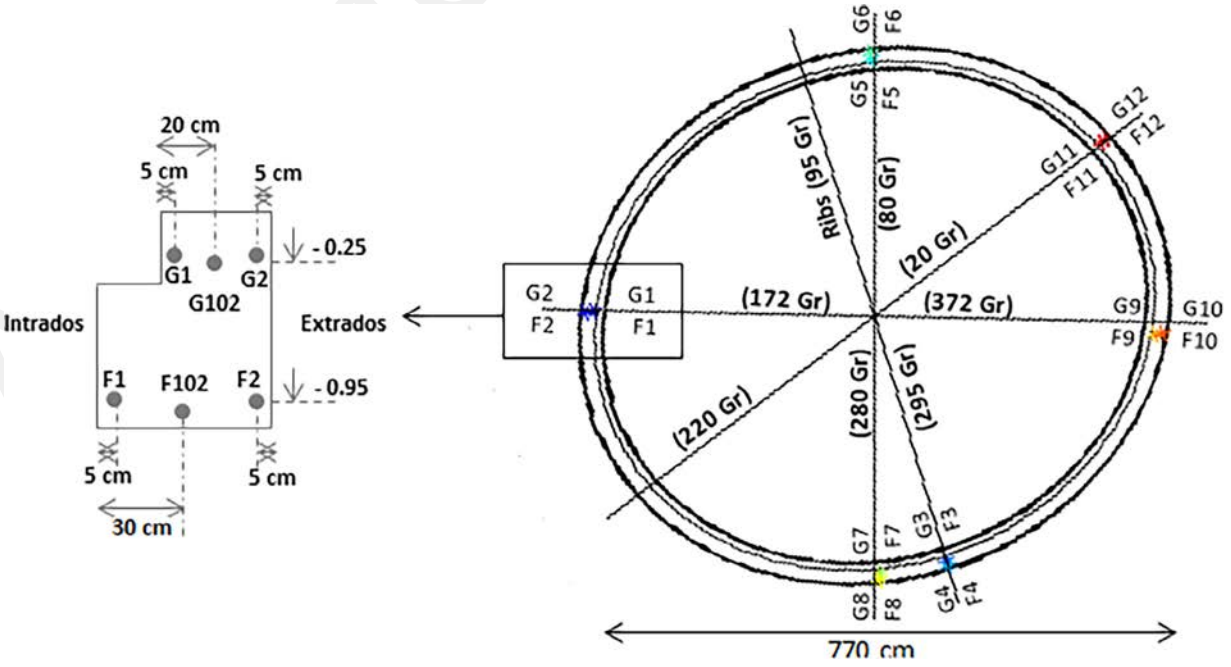

Fig. 3. Sensors' angular position and elevation in the VeRCoRs gusset (2D view from above).

Table 1
Observed coefficients of variation of temperature and strains at the gusset level.

Variable of Interest		Unit	Observed values				Observed values			
			Level −0.25 m				Level −0.95 m			
			min	max	mean	CoV (%)	min	max	mean	CoV (%)
Peak temperature (Early age)		°C	44	53	48	**06**	36	46	41	**06**
Peak strain (Early age)	T	μm/m	51	168	96	**34**	37	88	57	**31**
	V		176	270	232	**12**	87	201	127	**25**
Prestressing strain	T	μm/m	−41	−1	−16	**66**	−24	−0.5	−10	**87**
	V		−422	−52	−236	**64**	−202	−35	−112	**59**
Pressurization strain 0	T	μm/m	13	41	23	**36**	3	7	5	**24**
	V		7	229	98	**94**	6	106	52	**85**
Pressurization strain 1	T	μm/m	15	55	25	**45**	0.5	8.23	6	**40**
	V		12	239	100	**87**	5	111	54	**83**
Cracks' spacing	I	°	1.5	56	17	**82**	3.6	84	27	**82**
	E	°	5.5	95	21	**97**	4.2	95	20	**102**
Cracks' length	I	m	0.07	0.3	0.24	**31**	0.04	0.57	0.33	**48**
	E	m	0.1	0.3	0.20	**58**	0.03	0.54	0.22	**55**

T: Tangential – V: Vertical – I: Intrados – E: Extrados.

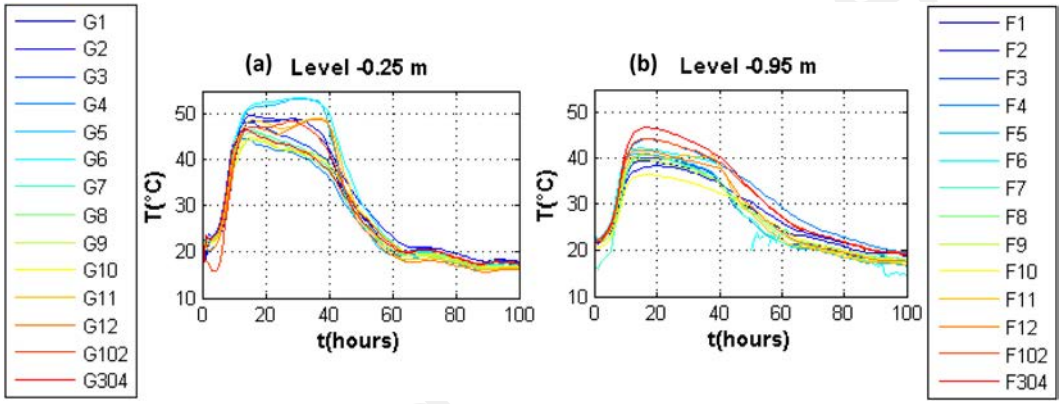

Fig. 4. Spatial variability of the temperature's evolution in time at the gusset for levels (a) −0.25 m and (b) −0.95 m.

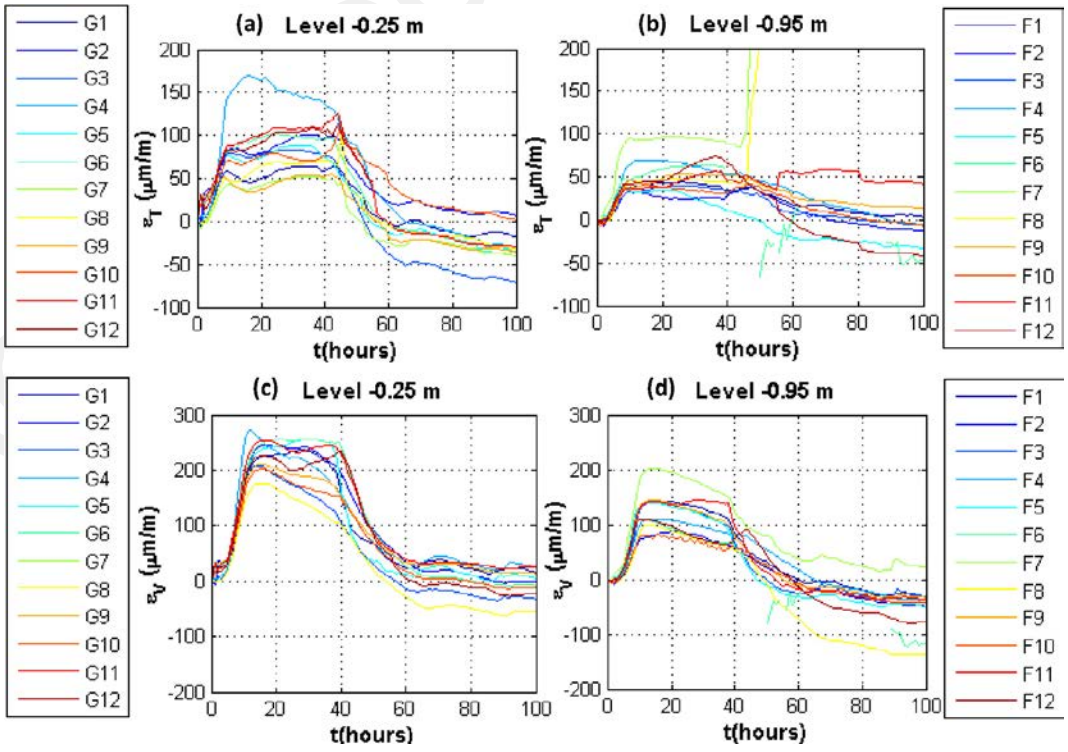

Fig. 5. Spatial variability of the (a & b) tangential and (c & d) vertical early age strains' evolution at the gusset for levels (a & c) −0.25 m and (b & d) −0.95 m.

compressed than the extrados as predicted by the numerical model (Bouhjiti et al., 2018). However, in the tangential direction, and for the F sensors (−0.95 m), in situ observations show no particular tendency with regards to the intrados and extrados behaviour. This differs from numerical results (Bouhjiti et al., 2018) where axisymmetric boundaries and restraining effects (more important in the vicinity of casting joints) lead to the same tangential strains for the F sensors. As stressed out in part I, such structural effects (variability of restraining effects along the gusset-base slab interface) are, generally, not known a priori. Also, the enhancement of the model's representativeness nearby the casting joint is conditioned by the implementation of an adapted behaviour law and adapted kinematic linkage allowing the introduction of spatially variable restraining loads along the gusset-base slab interface (which is beyond the scope of this contribution).

2.2. Global behaviour during the operational phase (OP)

During the operational phase, and as demonstrated numerically in Part I, the crack openings during the pressurization tests are controlled by the initial prestressing loads and the delayed prestressing losses. The variation of the first strain increment is related to the distribution of the prestressing cables around the sensor and the restraining effect of the base slab; whereas the second increment is dependent on three elements: the pressurization load, the restraining effects at the casting joint and, finally, the prestressing losses related to the viscoelastic behaviour (mainly creep and shrinkages) of concrete.

In the tangential direction (Fig. 6a & b), a strong variation of prestressing strain increment is observed (87% for the F sensors and 66% for the G sensors). However the measured values remain low and are of the same order of magnitude as the measuring precision (± 10 μm/m for the gauges and ± 20 μm/m when the temperature's precision ± 1°C is included). In addition, the prestressing effect does not seem to be correlated with the angular position of the sensor or with its distance from the anchorage zone (located in the ribs); in other words, the restraining effect seems to overcome the effect of instantaneous prestressing losses due to angular and linear frictions between the tendons and the concrete. Such restraining effects are also supposed to be responsible for the scattering of compressive strains between the intrados and extrados sides (as observed at early age) (Fig. 7).

In the vertical direction (Fig. 6c & d), a CoV around 60% is observed for both F and G sensors. The prestressing in this direction is unsurprisingly more efficient compared to the one in the tangential one (less restraining effect and less frictional losses). During the pressurization tests, measurements are not conclusive in the tangential direction: even though they show some scattering (CoV from 24% to 40% for the F sensors and from 36% to 45% for the G sensors), their values remain low (lower than the sensors' precision). However, in the vertical direction, the CoV are higher than 80% for both sensors F and G. This result is biased by the general tendency of the intrados and extrados behaviours: indeed during pressurization tests, tensile vertical strains develop rather on the intrados side and remain negligible on the extrados side. This is mainly due to the non-uniform vertical displacement in the gusset's cross section during prestressing and pressurization phases (which is opposed to the uniform displacement condition applied on the gusset's upper surface in Fig. 2c (Bouhjiti et al., 2018). It is worth mentioning that the choice of a uniform displacement in the vertical direction intends to prevent any unrealistic damage around the anchorage nodes in Fig. 2c. However, as underlined in part I, this strongly affects the vertical strain evolution and is not fully representative of the structural effects during prestressing and

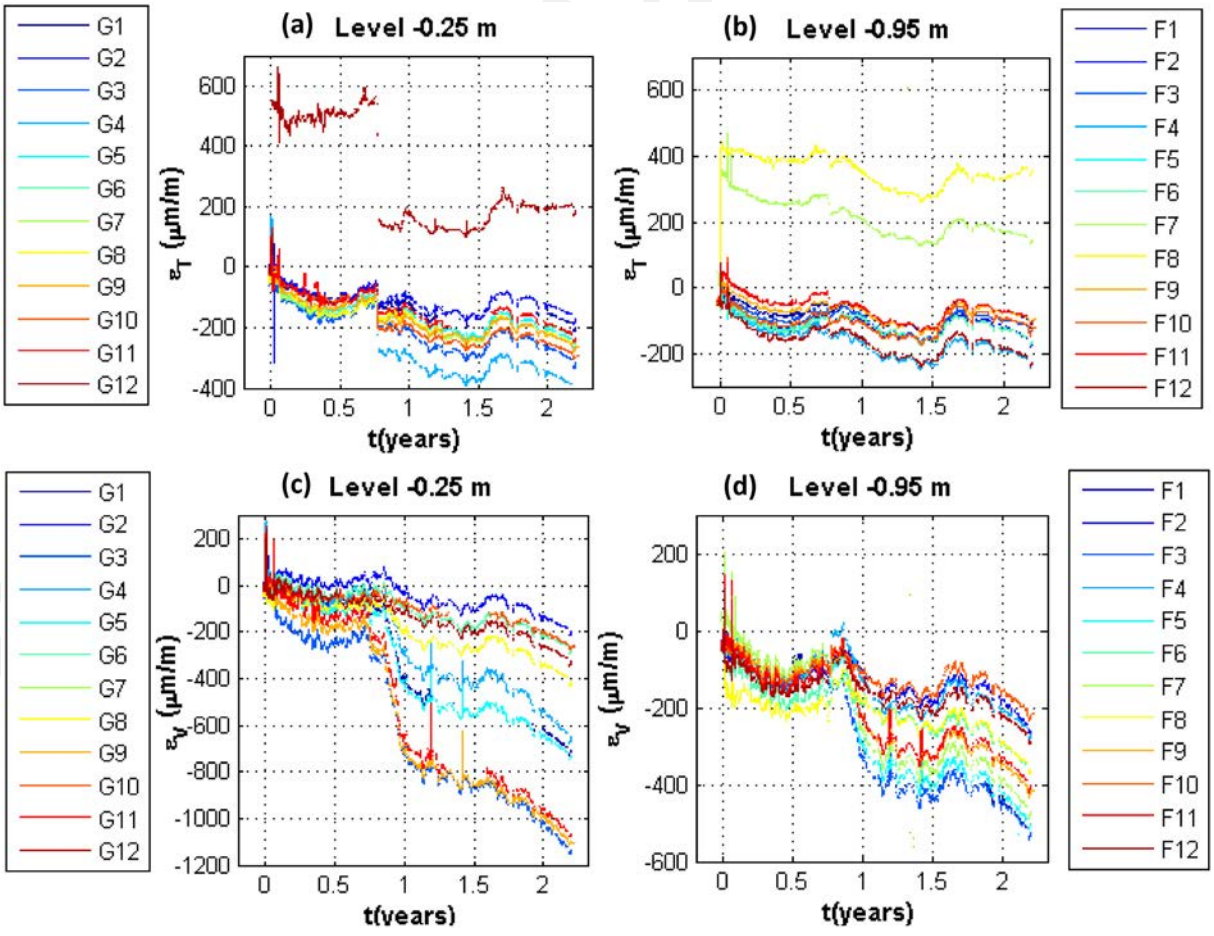

Fig. 6. Spatial variability of the (a & b) tangential and (c & d) vertical delayed strains' evolution at the gusset for levels (a & c) −0.25 m and (b & d) −0.95 m.

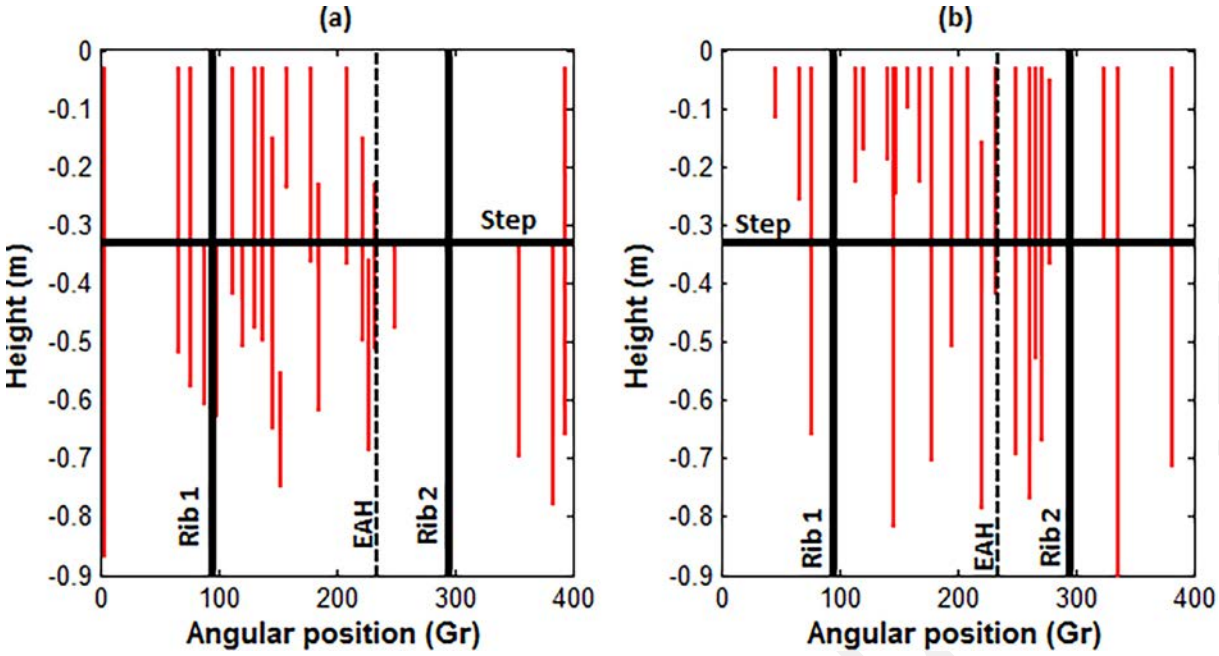

Fig. 7. In situ observations of cracks distribution at the gusset level (12 days after casting) (a) Extrados side (b) Intrados side.

pressurization phases.

One should also keep in mind that, numerically, the prestressing process is simplified compared to the one on site. Particularly: The prestressing sheath in which tendons are embedded and the post-tension cement grouted ducts are not modelled in Fig. 2b–d – The prestressing cables are modelled using 1D FE and are only activated during the mechanical calculations – The steel nodes and their coincident ones in concrete have the same displacement (perfect kinematic connection) – Prestressing loads are applied simultaneously and are computed as internal nodal forces. Despite such simplifying hypotheses, the simulated tangential behaviour in part I (direction of interest as cracks develop because of tangential restraining loads) remains accurate and representative of the one observed on site.

2.3. Cracking patterns

The observed cracking patterns at the gusset level are mainly obtained at early age (Fig. 6). The spacing values are not uniform and vary, in terms of angular position, from 1° to 95° along the gusset's circumference. Moreover, crack lengths are widely scattered and do not necessarily develop through the whole gusset's height. One can also notice that intrados and extrados cracking patterns are not perfectly matching. This questions the assumption of perfectly vertical through cracks and demonstrates the complexity of the cracking paths along the wall's thickness. Unfortunately, the visual observations cannot allow a clear identification of the through cracks nor define precisely their opening values (crackmeters precision less than100 μm).

From a numerical point of view, and based on simulations in part I (Bouhjiti et al., 2018), through cracks are vertical and develop along the whole gusset's height (for the considered mechanical properties at least – see Fig. 12c for illustration). The obtained crack opening values are also reasonable as they remain less than 100 μm. However, since the modelling is based on a 15° gusset RSV, spacing values per RSV cannot exceed 15°. For that reason, a post-processing of the various spacing values observed on site is required to define the frequency of the number of cracks per 15° revolution angle (this allows proper comparison between numerical results and experimental ones). As a result, in situ observations range from 0 to 3 cracks per 15° revolution angle. Thanks to the use of 30 RF realizations, two main modes have been identified numerically (1 and 2 cracks per RSV). The remaining ones (0 and 3 cracks per RSV) require higher number of realizations (which can become considerably expensive) or the consideration of other source of variation other than the spatial scattering of the Young's modulus. This is the main motivation behind the sensitivity analysis undertaken in the present contribution.

2.4. Discussion

One should keep in mind that the variation values in Table 1 are observed on the VeRCoRs gusset only and not necessarily on all double-walled NCBs gussets. On the one hand, the VeRCoRs mock-up has been extensively equipped with sensors which give access to a relatively representative number of measurement data to perform statistical analysis. This is not the case for the rest of NCBs where the number of sensors is considerably less and information is, accordingly, relatively restricted. On the other hand, structural effects might differ from one structure to the other; particularly from the 1:3 to the 1:1 scale and around the casting joints (strongly dependent on the casting quality, local concrete properties and local structural gusset-base slab interface linkage). Nevertheless, qualitatively, one should expect the same tendencies in terms of data scattering, intrados-extrados different behaviours, spatial variability of restraining effects along the gusset-bases lab interface and cracking random spacing values and lengths at early age.

One is also informed that the used THM model does not include any modelling of chemically induced damage and ageing (such as alkali–silica reaction, corrosion or environmentally induced deterioration of concrete). If required, such modelling can be achieved by enriching the various THM chains without modifying the suggested global strategy in part I (Bouhjiti et al., 2018) or the sensitivity analysis strategy in the present work.

Eventually, based on those observations, one can notice the complexity of the gusset's behaviour and the importance of including the various inputs' variability to accurately reproduce the observed variability related to in-situ measurements and structural effects. Despite the limitations of the suggested modelling strategy, its ability to reproduce accurately concrete cracking modes encourages its use and justifies the interest in the model's sensitivity analysis. Hence, the purpose of the forthcoming paragraphs is to identify the possible origins of the observed on site variations with an attempt to answer two key questions:

– Based on the FE analysis strategy suggested in part I (Bouhjiti et al., 2018) (Figs. 1 and 2), what are the influential parameters that affect the most the model's response and, accordingly, the behaviour of concrete?
– How do such variations affect the cracking patterns during both the pre-operational and operational phases?

3. Global sensitivity analysis strategy

The used Global Sensitivity Analysis (GSA) is based on the distinction of the Pre-Operational and Operational phases (POP and OP) as shown in Part I (Fig. 1) and illustrated in Fig. 8.

The sensitivity analysis covers, first, one calculation step at a time and the uncertainties propagation deals only with the most influential parameters identified for each step. For instance: at early-age the most important factors affecting concrete's thermal behaviour are identified first. Then, they are used as a part of the sensitivity analysis of the mechanical behaviour along with the rest of the mechanical inputs. This allows a multi-layered analysis covering both intermediate results such as the temperature and strain profiles before dealing with the ultimate variable of interest which is the cracking pattern.

Practically, the sensitivity analysis consists of performing a 1st order variance-based approach (Sobol, 2001) using the OFAT method. In that sense, the various parameters are supposed independent. This strong hypothesis is considered as a first step before performing in-depth and higher order analyses between the most influential parameters. Indeed, the priority for correlation investigation should be granted to parameters with important effects.

For a given variable of interest (one of the T-H-M model's output) Y, the reference response is denoted Y_0. It is obtained using the mean values $X^Y_{i,0}$of the various inputs X^Y_i associated with the model Y. For a given input X^Y_i, the min and max values are denoted $X^Y_{i,-}$ and $X^Y_{i,+}$ respectively and the lower and upper bonds of the model's response are denoted $Y^-_{X_i}$ and $Y^+_{X_i}$. The variance-based method consists of computing a global sensitivity index $\delta^Y_{X_i}$describing the portion of variance induced by the variation of the i-th parameter compared to the total one due to all parameters variation (Sobol, 2001). This writes in the case of independent inputs (Eq. (1)):

$$0\% \leqslant \delta^Y_{X_i} = \frac{\mathrm{Var}[Y^-_{X_i}, Y_0, Y^+_{X_i}]}{\sum_j \mathrm{Var}[Y^-_{X_j}, Y_0, Y^+_{X_j}]} \leqslant 100\% \tag{1}$$

with $\mathrm{Var}[Y^-_{X_i}, Y_0, Y^+_{X_i}]$ is the variance of given values $\{Y^-_{X_i}, Y_0, Y^+_{X_i}\}$of the model's response.

The sorting of the obtained values leads to an ordered listing of the most influential parameters. It is worth noting that, by definition, the index above is subjective and strongly depends on the selected inputs' CoV. For instance, a given parameter X_1 can be less important than another one X_2 when both have the same coefficients of variation $CoV_1 = CoV_2$. However by increasing CoV_1, X_1might appear more influential than X_2. Therefore, it is important for the variation domains to be as realistic as possible to approach objectivity from a physical point of view (mathematically, objectiveness requires the normalization of the $\delta^Y_{X_i}$ index or the use of equal CoVs). In our case, physical objectiveness is preferred based on experimental measurements or expert judgment. If the CoV is unknown for a given parameter, it is fixed according to the rest of the observed CoVs to ensure, at least, a mathematical objectiveness.

The previous index $\delta^Y_{X_i}$ does not allow the identification of the observed gaps from the reference analysis. For such partial analysis, other 1st order sensitivity indexes can be considered (CoV^Y_i and $\overline{CoV^Y_i}$ in, Eq. (2)).

$$\overline{CoV^Y_i} = \frac{CoV^Y_i}{CoV^X_i} \qquad CoV^X_i = \frac{\sqrt{\mathrm{Var}[X^Y_{i,-}, X^Y_{i,0}, X^Y_{i,+}]}}{\mathrm{Mean}[X^Y_{i,-}, X^Y_{i,0}, X^Y_{i,+}]} \quad CoV^Y_i = \frac{\sqrt{\mathrm{Var}[Y^-_{X_i}, Y_0, Y^+_{X_i}]}}{\mathrm{Mean}[Y^-_{X_i}, Y_0, Y^+_{X_i}]} \tag{2}$$

with Var and Mean are the variance and average of a given set of values. $\overline{CoV^Y_i}$ is the normalized CoV defined as the ratio of the model's coefficient of variation CoV^Y_i to the one of the input CoV^X_i.

Compared to other OFAT methods (the Cotter method for instance (Cotter, 1979), the suggested sensitivity analysis has the advantage of describing a variation around the reference response with the least number possible of simulations (2∗N + 1 with N number of parameters). This allows (a) writing the variance of a given variable of interest as the sum of variances due to most influential parameters (Eq. (3)) and (b) defining an approximation of the Response Surface RS for

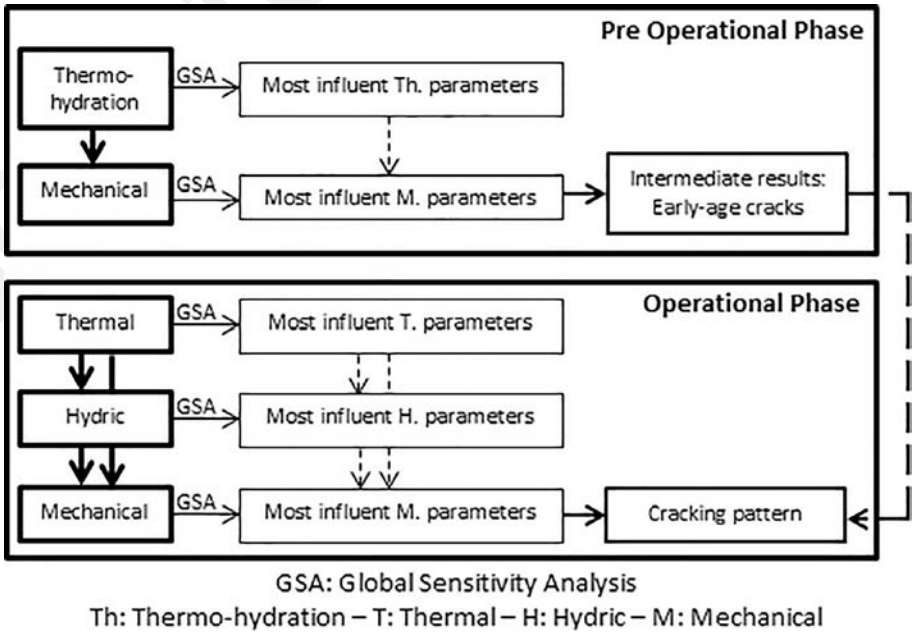

Fig. 8. General 1st order GSA of concrete cracking under simultaneous THM loads.

their variation domains depending on the observed variation of the model's response (Eq. (4)).

$$\mathrm{Var}(Y) \geqslant \sum_{i=1}^{N' \leqslant N} \mathrm{Var}[Y_{X_i}^{-}, Y_0, Y_{X_i}^{+}] \tag{3}$$

$$\mathrm{CoV}^{Y} \geqslant \sqrt{\sum_{i=1}^{N' \leqslant N} (\overline{\mathrm{CoV}_i^{Y}}\,\mathrm{CoV}_i^{X})^2} \tag{4}$$

where N is the number of inputs involved to compute the variable of interest Y and N' is the reduced number of most influential parameters. CoV^{Y} is the CoV associated with the response Y as a result of all inputs' variations.

By inverse analysis, and based on the observed variation of the output Y denoted $\mathrm{CoV}^{Y,EXP}$, one can approximate the realistic variation domains of most influential parameters $\mathrm{CoV}_i^{X,EXP}$:

$$\mathrm{CoV}^{Y,EXP} \geqslant \sqrt{\sum_{i=1}^{N' \leqslant N} (\overline{\mathrm{CoV}_i^{Y}}\,\mathrm{CoV}_i^{X,EXP})^2} \tag{5}$$

where $\mathrm{CoV}^{Y,EXP}$ known a posteriori thanks to in situ measurements and $\overline{\mathrm{CoV}_i^{Y}}$ computed numerically based on the 1st order OFAT sensitivity analysis.

4. Identification of the most influential parameters in the THM model

4.1. Variation domains of inputs and variables of interest

4.1.1. Thermo-hydration and thermal parameters

The descriptive equations of concrete's thermo-hydration are summed up as following (Bouhjiti et al., 2018):

$$\text{Heat equation:}\begin{cases} \frac{d}{dt}\left(\int_{T_0}^{T} \rho_c C_c^p(r)dr\right) - \nabla\cdot(\lambda_c \nabla T) = Q_\infty \frac{d\alpha}{dt} e^{-\frac{E_a^{th}}{RT(t)}} \\ \lambda_c = (1.33-0.33\alpha)(1 + k_\lambda(T-T_{ref}^{th}))\lambda_{hc}(T_{ref}^{th}) \\ C_c^p = (1-k_{C^p}(T-T_{ref}^{th}))C_{hc}^p(T_{ref}^{th}) + (1-\alpha)k_{bw}\frac{c_0}{\rho_c}\varsigma_\infty C_w^p \end{cases}$$

$$\text{BC:}\begin{cases} \mathbf{q_{th}}.\,\mathbf{n} = h_{eq}(T-T_{ext}) \\ h_{eq} = \left(\frac{1}{h_{conv}} + \sum_i \frac{e_i}{\lambda_i}\right)^{-1} \end{cases} \tag{6}$$

where ρ_c is the concrete's density (kg/m^3), C_c^p is the concrete's thermal capacity (J/kg/°K), λ_c is the concrete's thermal conductivity (J/s/m/°K), Q_∞ is the volumetric hydration heat (J/m^3), $\widetilde{A}(\alpha) = \frac{d\alpha}{dt}$ is the chemical affinity associated with the hydration reaction and normalized hydration rate $\alpha = \frac{\varsigma}{\varsigma_\infty}$, E_a^{th} is the apparent activation energy associated with the hydration process (J/mol), ς is the hydration rate defined as the ratio of the hydrated cement mass to the initial cement mass, ς_∞ is the ultimate hydration rate, R is the universal gas constant (8.314 J/°K/mol), $\lambda_{fc}(C_{fc}^p)$ and $\lambda_{hc}(C_{hc}^p)$ are the thermal conductivity (thermal capacity) of fresh and hardened concrete respectively, C_w^p is the thermal capacity of water (4186 J/kg/°K), k_{bw} is a factor depending on the chemical composition of the used cement, k_λ (between 0.0006 for siliceous aggregates and 0.0015 for calcareous type) and k_{C^p} (between 0.0007 for siliceous aggregates and 0.0016 for calcareous type) are the associated slope factors (/°C), T_{ref}^{th} is the reference temperature at which the identification is made, h_{eq} is the exchange coefficient (J/s/m^2/°K), h_{conv} is the equivalent exchange coefficient including all modes of heat exchange, e_i is the thickness of protective layers (m) and λ_i is the thermal conductivity of the protective layer (J/s/m/°K).

The observed variation of concrete's density ρ_c (18 measurements) is limited to 2% (Corbin and Garcia, 2015) reflecting a rather precise mixing process. The variations of the other inputs in the heat equation are issued from previous works: in the case of thermal capacity C_c^p (Commission-CEA, 1981) and thermal conductivity λ_c (Neville, 2004) a variation of 40% is considered to illustrate the eventual effects of temperature and initial water content. The temperature and hydration

Table 2
Variation domains of the considered main thermal inputs.

	Symbol	Unit	Domain of variation				Refs.
			Reference	Min	Max	CoV (%)	
Th. and T. parameters	C_{hc}^p	J/kg/°K	880	528	1232	**40**	Commission-CEA (1981)
	λ_{hc}	J/s/m/°K	1.87	1.12	2.62	**40**	Neville (2004)
	Q_∞	J/m^3	$8.5{\cdot}10^7$	$5.1{\cdot}10^7$	$1.2{\cdot}10^8$	**40**	Corbin and Garcia (2015), Taylor (1997), Waller (1991), Schindler and Folliard (2005)
	E_a^{th}	J/mol	26 10^3	16 10^3	36 10^3	**40**	–
	k_λ	/°C	0.001	0	0.0015	**92**	Bouhjiti et al. (2018)
	$\lambda_{hc}(\Delta T = 30°C)$	*J/s/m/°K*	*1.92*	*1.87*	*1.95*	*02*	
	k_{C^p}	/°C	0.001	0	0.0016	**93**	
	$C_{hc}^p(\Delta T = 30°C)$	*J/kg/°K*	*906*	*880*	*837*	*04*	
	Hydration effect		YES	NO	YES	-	–
	λ_{hc} (J/s/m/°K)		*2.48 → 1.87*	*1.87*	*2.48 → 1.87*	**20**	
	C_{hc}^p (J/kg/°K)		*992 → 880*	*880*	*992 → 880*	**08**	
T. loads	λ_{fw}	J/s/m/°K	0.5	0.21	0.84	**61**	Powers and Brownyard (1946)
	h_{eq}	*J/s/m^2/°K*	*5.81*	*3.68*	*7.00*	**30**	
	h_{conv}	J/s/m^2/°K	10	6	15	**43**	Briffaut et al. (2012)
	h_{eq}	*J/s/m^2/°K*	*5.81*	*4.19*	*7.21*	**26**	
	T_{ext}	°C	20	12	28	**40**	–
	T_{ref}^{th}	°C	20	12	28	**40**	–
	T_{heat}	°C	$T_{ext}+30$	$T_{ext}+42$	$T_{ext}+18$	**40**	–

Values in *grey* and italic are indirect parameters deduced from direct ones in black.

effects have a smaller effect on concrete thermal properties (less than 20%) compared to their intrinsic variation estimated at 40%. As for the hydration heat Q_∞, the identified value from the adiabatic test (reference value) is 40% less than the one estimated using theoretical approaches (Taylor, 1997; Waller, 1991; Schindler and Folliard, 2005). Such differences can be due to the heat losses during the supposedly perfect adiabatic tests and also the variation of the cement content in the considered volume of concrete. One is reminded that the identification of the hydration heat involves the use of the thermal capacity; however, the considered 40% variation is, in the case of Q_∞, representative of the variation of the ultimate temperature during the adiabatic test and not the variation of the thermal capacity. The chemical affinity $\widetilde{A}(\alpha)$ is considered constant as it mainly depends on the cement type which does not change.

The boundary conditions are also varied up to 40%: for the convective exchange factor h_{conv} this variation can be observed for low wind velocities (less than 20 km/h) and thermal gradients between the surface of concrete and the ambient air up to 80 °C (Briffaut et al., 2012). Finally, the service $T_{ext} = T_{serv}$ and unit outage temperatures $T_{ext} = T_{test}$ variation is arbitrarily set to 20% in accordance with the hydric properties variations.

A summary of these variations is provided in Table 2.

For this calculation step, the variables of interest are: The maximal temporal thermal gradient responsible for concrete thermal shrinkage and the hydration kinetic defining the evolution of the endogenous shrinkage and concrete's maturity.

4.1.2. Drying parameters

The drying problem writes (Bouhjiti et al., 2018):

$$\text{Heat equation:}\begin{cases}\dot{C}_w = \nabla\cdot(D_w\nabla C_w)\\ D_w(C_w,T) = A_w e^{B_w C_w}\frac{T}{T^{dr}_{ref}}e^{-\frac{E^W_a}{R}\left(\frac{1}{T}-\frac{1}{T^W_{ref}}\right)}\end{cases}$$

$$\text{BC:}\begin{cases}\mathbf{q_w}\cdot\mathbf{n} = h_w(RH-RH_{ext})\\ RH_{ext} = 163.61\frac{r}{r+0.62}e^{-\frac{17.5T_{ext}}{241.2+T_{ext}}}\end{cases}$$

$$\text{Desorption curve:}\frac{C_w}{C_{w,0}} = S_r = \left(1+(-a_w\ln(RH))^{\frac{1}{1-b_w}}\right)^{-b_w} \quad (7)$$

where D_w is the water diffusivity factor (m^2/s), C_w is the water content ($litr/m^3$), (A_w,B_w) are two parameters adjusted according to the experimental results of water loss, T^W_{ref} is the reference temperature at which the drying test is performed (°K), E^W_a is the activation energy associated with the drying phenomena, h_w is the hydric exchange coefficient, RH_{ext} is the ambient RH, $C_{w,0}$ is the water content available for drying after the end of the hydration process, a_w,b_w are fitting parameters identified from the experimental desorption curves and S_r the saturation ratio.

The initial water content $C_{w,0}$in concrete depends on the estimated hydration rate which can vary from 75% to 100% depending on the used theoretical expression (Mills, 1966; Issadi et al., 2016). This leads to an eventual maximum 15% gap between the possible values. In the considered model, only the desorption curve is retained. However, sorption and desorption curves do not coincide. This means that the parameters a_w and b_w differ in the cases of drying and wetting cycles. A 20% variation is considered herein based on existing experimental results (mainly of the intrinsic spatial scattering of hydric behaviour in Granger (1995)). As for the diffusivity parameters in D_w a variation of 34% is observed (Mazars et al., 2015) for different concrete types in the case of parameter A_w. For the remaining parameters, the quantification of their associated CoV is lacked (both for the VeRCoRs concrete and in the explored literature work). As a compromise, a value of 20% variation is retained for all hydric parameters. This value is representative of the physical variability for parameters $C_{w,0}$,a_W,b_W,A_w and ensures an objective evaluation of the effect of the remaining parameters of which the physical CoV are unknown precisely. In particular, for the same CoVs, the variation of B_w, being a power factor, is expected to have more effect on the diffusivity factor $D_w$and the model's response compared to A_w. In (Mazars et al., 2015), it is recommended that B_w should be fixed at 0.05 (to ensure physical representativeness) and that A_w should be fitted to experimental results. However, an applied variation of 20% for B_w still provides reasonable and physically acceptable values of the diffusivity factor. Therefore, $B_w$is considered herein variable which should restrain less the fitting process and allow better adjustments.

The variation of the hydric boundaries (ambient relative humidity RH_{ext}) is directly related to the variation of the ambient temperature and mix ratio r during POP and OP. A maximum variation of 40% is obtained when the service temperature varies by 20%.

Table 3 presents the variation of each hydric parameter.

The variables of interest are the saturation ratio and the relative humidity as they directly affect concrete's mechanical behaviour (creep and drying).

4.1.3. Mechanical and size effect parameters

The mechanical model used within the present study is recalled through Fig. 9 (creep model), Eq. (8) (unilateral damage model) and Eq. (9) (Statistical Size Effect Law SSEL in terms of the damage threshold) (Bouhjiti et al., 2018).

Table 3
Variation domains of the considered main hydric inputs.

	Symbol	Unit	Domain of variation				Ref.
			Reference	Min	Max	CoV (%)	
H. parameters	$C_{w,0}$	l/m^3	132	105	158	**20**	Mills (1966), Issadi et al. (2016)
	E^w_a	J/mol	$39{\cdot}10^3$	$31{\cdot}10^3$	$47{\cdot}10^3$	**20**	–
	T^W_{ref}	°C	20	16	24	**20**	–
	B_w	–	0.05	0.04	0.06	**20**	–
	A_w	m^2/s	$3.1{\cdot}10^{-12}$	$2.5{\cdot}10^{-12}$	$3.7{\cdot}10^{-12}$	**20**	Mazars et al. (2015)
	a_w	–	7.6	6.1	9.1	**20**	Granger (1995)
	b_w	–	0.33	0.26	0.39	**20**	
H. loads	h_w	m/s	$3.415{\cdot}10^{-9}$	$2.732{\cdot}10^{-9}$	$4.098{\cdot}10^{-9}$	**20**	–
	r	g/kg	6.31	5.04	7.57	**20**	–
	RH_{ext}	%	*20*	*14*	*21*	***20***	
	T_{serv}	°C	35	28	42	**20**	–
	RH_{ext}	%	*20*	*27*	*12*	***38***	
	T_{test}	°C	20	16	24	**20**	–
	RH_{ext}	%	*43*	*55*	*34*	***24***	

Values in *grey* and italic are indirect parameters deduced from direct ones in black.

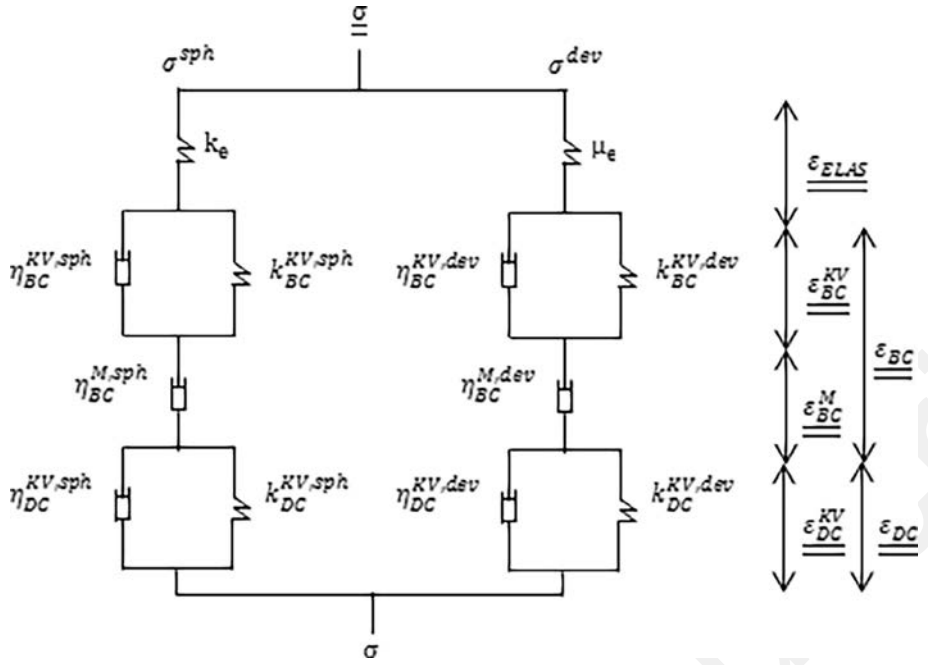

Fig. 9. Rheological model for concrete basic and drying creep where k_e,μ_e are the bulk and shear moduli respectively (defined from the Young's modulus E and the elastic Poisson ratio ν_{ELAS}), η^{KV},k^{KV},η^{M}represents the rheological model components (Bouhjiti et al., 2018).

$$\boldsymbol{\varepsilon_{TOT}} = \boldsymbol{\varepsilon_{ELAS}} + \boldsymbol{\varepsilon_{TH}} + \boldsymbol{\varepsilon_{ES}} + \boldsymbol{\varepsilon_{DS}} + \boldsymbol{\varepsilon_{CR}}$$

$$\text{Behaviour law:} \begin{cases} \boldsymbol{\sigma} = (1-d)\mathbf{C_0}:\boldsymbol{\varepsilon} \\ d = 1-(1-A_t)\frac{Y_0}{Y_t} - A_t e^{-B_t(Y_t-Y_0)} \\ Y_t = \sup(\varepsilon_{\mu 0,t}, \max(\varepsilon_{eq,t})) \end{cases}$$

$$\text{Damage}-\text{creep coupling: } \{\varepsilon_{eq,t} = ||\boldsymbol{\varepsilon_{ELAS}} + \beta_{coupl}\boldsymbol{\varepsilon_{CR}}||_t$$

$$\text{Crack opening: } w_{ck} = h_{EF}\, d(||\boldsymbol{\varepsilon_{ELAS}}|| + ||\boldsymbol{\varepsilon_{CR}}||) \tag{8}$$

where $\boldsymbol{\varepsilon_{TOT}}$ is the total strain tensor divided into five main components: $\boldsymbol{\varepsilon_{ELAS}}$ is the elastic strain tensor, $\boldsymbol{\varepsilon_{TH}} = \alpha_{th}(T-T_0)\mathbf{I_d}$ the thermal strain tensor associated with the temperature variation, $\boldsymbol{\varepsilon_{ES}} = \alpha_{ES} < \alpha-\alpha_0 >_+ \mathbf{I_d}$ is the endogenous shrinkage tensor induced by the water consumption during hydration with α_0 the percolation threshold, $\boldsymbol{\varepsilon_{DS}} = \alpha_{DS}(C_w-C_{w,0})\mathbf{I_d}$is the drying shrinkage tensor caused by water content variation and $\boldsymbol{\varepsilon_{CR}}$ is the creep strain tensor (sum of basic $\boldsymbol{\varepsilon_{BC}}$and drying creeps $\boldsymbol{\varepsilon_{DC}}$). α_{th} (/°K), α_{ES} and α_{DS} are the coefficients of thermal, endogenous and drying shrinkages respectively. $\mathbf{I_d}$ is the identity tensor and $<X>_+ = \max(X;0)$. $\mathbf{C_0}$ is the initial compliance tensor (undamaged d = 0), d the damage variable, A_t and B_t are numerical parameters defining the post-peak tensile behaviour law, $\varepsilon_{\mu 0,t}$ is the tensile damage thresholds, $\varepsilon_{eq,t}$ the equivalent strain (scalar) based on the 1st and 2nd tensor's invariants (De Schutter and Taerwe, 1996), β_{coupl} is the coupling factor between damage and creep. $h_{EF} = \sqrt[3]{V_{EF}}$ is the characteristic length of the finite element that has a volume of V_{EF} and $||X|| = \max(X_I,X_{II},X_{III},0)$ with X_I,X_{II},X_{III} are the Eigen values of a given tensor X.

$$\text{SSEL:}\mathbb{H}_{\varepsilon_{\mu 0,t}} = \left[\left(\frac{\sqrt[3]{\int_\Omega e^{-\pi\left(\frac{|x-x_0|}{D_{str,0}}\right)^2} d\Omega}}{D_{ref}}\right)^{-\frac{3}{m}} R_{t,ref}\right](\mathscr{L}og_E)^{-1} \tag{9}$$

where $\mathbb{H}_{\varepsilon_{\mu 0,t}}$ is the resulting RF associated with the damage threshold $\varepsilon_{\mu 0,t}$, $D_{str,0}$ and D_{ref} are respectively the characteristic structural and reference sizes, m is the Weibull modulus associated with the tensile strength distribution at the reference scale $R_{t,ref}$ ($m \approx \frac{1.2}{CoV_{R_t}} + 0.2$), Log_E is the spatially correlated lognormal RF descriptive of the Young's modulus spatial scattering (requiring the mean value $\mu = E_{hc}$, the CoV = CoV_E and the covariance matrix $C(\vec{x},\vec{x_0}) = \sigma_E^2\rho_{ac}(\vec{x},\vec{x_0},l_{ac})$as inputs). σ_E^2 is the Young's modulus variance, ρ_{ac} is the considered autocorrelation function and l_{ac} is the autocorrelation length (Bouhjiti et al., 2018).

Based on several measurements (more than 50) performed on the VeRCoRs's concrete mechanical properties (Corbin and Garcia, 2015), the Young's modulus E_{hc}, the tensile strength $R_{t,hc}$, the fracture energy G_F and the compressive strength $R_{c,hc}$ show a variation of 10%. According to the maturity method, the evolution of the mechanical properties at early age writes: $X = \left(\frac{\alpha-\alpha_0}{1-\alpha_0}\right)^{b_X} X_{hc}$. The early-age associated power factors $b_{X\in\{E,R_t,R_c,G_F\}}$ and percolation threshold α_0 variations are set to 50% based on experimental results in Torrenti and Benboudjema (2005), Charpin et al. (2015). As for the viscoelastic properties in Fig. 9 (Powers and Brownyard, 1946), the Poisson ratios (Charpin et al., 2015) and the endogenous α_{ES} and drying shrinkage α_{DS} coefficients (basic and drying creep parameters), their CoV are defined in accordance with the probabilistic analyses in Berveiller et al. (2012), de Larrard (2010).

Being still a subject of controversy, size effects parameters (Table 4) are considered highly uncertain in our analysis; for that reason their CoV are set to 50%. For the fluctuation length l_{flu} (Sellier and Millard, 2014); (de Larrard et al., 2010) and the objective scale length $D_{str,0}$ (Ghannoum et al., 2017); (Foucault et al., 2012) such variations are supported by experimental results scattering. As a result, the 50% variation of the objective scale length leads to about 10% variation of the tensile strength at the structural scale (the same value is observed for its intrinsic variation around the mean value) whereas a 50% variation of the tensile strength's CoV induces 60% variation of the Weibull modulus m and more than 20% of its value at the structural scale. Accordingly, the Weibull modulus is expected to have more influence on the observed cracking patterns compared to the rest of size effects parameters.

Finally, the mechanical loads variation is directly issued from onsite observations in Table 1. The variation of the prestressing loads is set to 50% due to various instantaneous prestressing losses and restraining effects. The pressurization loads variation is also set to 50% based on observations in Table 1. The reference values, however, account for the restraining effects due to the presence of the base slab (the effective

Table 4
Variation domains of the considered main mechanical inputs.

	Symbol	Unit	Domain of variation				Refs.
			Reference	Min	Max	COV (%)	
Viscoelastic parameters	α_0	%	15	7.5	22.5	**50**	Charpin et al. (2015)
	α_{TH}	m/m/°C	$10{\cdot}10^{-6}$	$9{\cdot}10^{-6}$	$11{\cdot}10^{-6}$	**10**	–
	α_{ES}	m/m	$74{\cdot}10^{-6}$	$67{\cdot}10^{-6}$	$81{\cdot}10^{-6}$	**10**	Berveiller et al. (2012)
	α_{DS}	m/m/(l/m^3)	$7.1{\cdot}10^{-6}$	$6.4{\cdot}10^{-6}$	$7.8{\cdot}10^{-6}$	**10**	
	E_{hc}	Pa	$36{\cdot}10^{9}$	$32{\cdot}10^{9}$	$40{\cdot}10^{9}$	**10**	Corbin and Garcia (2015)
	b_E	–	0.81	0.4	1.2	**50**	Torrenti and Benboudjema (2005)
	$\nu_{ELAS,hc}$	–	0.2	0.1	0.3	**50**	–
	ν_{BC}	–	0.2	0.1	0.3	**50**	Berveiller et al. (2007)
	ν_{DC}	–	0.3	0.15	0.45	**50**	
	$\eta_{BC,0}^{KV,dev}$	Pa	$2.3{\cdot}10^{17}$	$1.8{\cdot}10^{17}$	$2.7{\cdot}10^{17}$	**20**	Berveiller et al. (2012), Larrard (2010)
	$k_{BC,0}^{KV,dev}$	Pa.s	$6.29{\cdot}10^{10}$	$5{\cdot}10^{10}$	$7.5{\cdot}10^{10}$	**20**	
	$\eta_{BC,0}^{M,dev}$	Pa	$4.4{\cdot}10^{18}$	$3.5{\cdot}10^{18}$	$5.3{\cdot}10^{18}$	**20**	
	$eta_{DC,0}^{KV,dev}$	Pa.s	$9.1{\cdot}10^{3}$	$7.3{\cdot}10^{3}$	$1.1{\cdot}10^{4}$	**20**	
	$k_{DC,0}^{KV,dev}$	Pa.s/s	$2.6{\cdot}10^{9}$	$2.1{\cdot}10^{9}$	$3.1{\cdot}10^{9}$	**20**	
	κ	Pa	8.28 10^{-4}	$6.6{\cdot}10^{-4}$	$9.9{\cdot}10^{-4}$	**20**	
	T_{ref}^{CR}	°C	20	16	24	**20**	–
	$E_a^{KV} = E_a^{M}$	–	$25{\cdot}10^{3}$	$20{\cdot}10^{3}$	$30{\cdot}10^{3}$	**20**	–
Damage and size effects parameters	$R_{c,hc}$	Pa	$48{\cdot}10^{6}$	$43{\cdot}10^{6}$	$53{\cdot}10^{6}$	**10**	Corbin and Garcia (2015)
	b_{Rc}	–	0.74	0.37	1.11	**50**	Torrenti and Benboudjema (2005)
	$R_{t,hc,ref}$	Pa	4.5 10^{6}	4 10^{6}	5 10^{6}	**10**	Corbin and Garcia (2015)
	$R_{t,hc,str}$	*Pa*	*$2.9{\cdot}10^{6}$*	*$2.6{\cdot}10^{6}$*	*$3.2{\cdot}10^{6}$*	**10**	
	b_{Rt}	–	0.84	0.42	1.26	**50**	Torrenti and Benboudjema (2005)
	$G_{F,hc}$	N/m	77	69	85	**10**	Corbin and Garcia (2015)
	b_{GF}	–	0.84	0.42	1.26	**50**	Torrenti and Benboudjema (2005)
	β_{coupl}	%	40	20	60	**50**	–
	$D_{str,0}$	m	1	0.5	1.5	**50**	Ghannoum et al. (2017), Foucault et al. (2012)
	$R_{t,hc,str}$	*Pa*	*2.9 10^{6}*	*$2.7{\cdot}10^{6}$*	*$3.2{\cdot}10^{6}$*	***08***	
	$CV_{Rt} = \frac{\sigma_{Rt}}{\mu_{Rt}}$	%	10	5	15	**50**	–
	m	–	*12*	*24*	*8*	**60**	
	$R_{t,hc,str}$	*Pa*	*2.9 10^{6}*	*$2.2{\cdot}10^{6}$*	*$3.6{\cdot}10^{6}$*	***25***	
	$l_{flu,E}$	m	1	0.5	1.5	**50**	de Larrard et al. (2010), Sellier and Millard (2014)
	$CV_E = \frac{\sigma_E}{\mu_E}$	%	10	5	15	**50**	–
M. loads	σ_{PREC}^{V}	Pa	$8.5{\cdot}10^{6}$	$4.2{\cdot}10^{6}$	$12.7{\cdot}10^{6}$	**50**	Table 1
	σ_{PREC}^{T}	Pa	$1{\cdot}10^{6}$	$0.5{\cdot}10^{6}$	$1.5{\cdot}10^{6}$	**50**	
	σ_{PRES}^{V*}	Pa	$2.5{\cdot}10^{6}$	$1.25{\cdot}10^{6}$	$3.7{\cdot}10^{6}$	**50**	
	σ_{PRES}^{T*}	Pa	$0.5{\cdot}10^{6}$	$0.25{\cdot}10^{6}$	$0.75{\cdot}10^{6}$	**50**	

Values in *grey* and italic are indirect parameters deduced from direct ones in black - * restraining effects accounted for.

tangential stress during pressurization has been estimated in Bouhjiti et al., 2018 to be 90% less than the value without the base slab $\sigma_{PRES}^{T*} = 0.1*\left(\frac{R_{int}}{e} + \frac{1}{2}\right)\Delta P$ with ΔP the applied inner pressure, R_{int} the inner radius, e the thickness of the gusset). One is reminded that the applied pressurization loads ΔP are rather well monitored on site. The observed variability of vertical and tangential strains increment (during pressurization) in Table 1 is related to the structural effects (non-uniform vertical displacement and non-uniform tangential restraining loads) and to local effects (mainly the existence of damage areas and macrocracked zones). Within the used model, local effects are fully modelled and their effect on the computed strain can be quantified though the applied inner pressure is constant (for example it is shown in part I (Bouhjiti et al., 2018) that the presence of cracks leads to 50% - 350% variation of tangential strains depending on the distance from the crack). However, the previous structural effects are partially accounted for. In that sense, the used CoVs are representative (explicitly) of the effects of such structural effects on the RSV's response.

In addition to the physical parameters cited beforehand, the effect of the autocorrelation function's shape is also studied hereafter. With that regard, three functions are considered as shown in Table 5 (Bouhjiti et al., 2018): the linear, the Gaussian and the sinusoidal functions. For objectivity purposes, their respective autocorrelation lengths l_{ac} are modified using the so-called fluctuation length $l_{flu} = \int_{-\infty}^{+\infty} \rho_{ac}(u,l_{ac})du$ (Bouhjiti et al., 2018). One can notice that, for the same fluctuation length, and compared to the linear function, the autocorrelation length is less important for the Gaussian and sinusoidal functions in that order. Also, as the sinusoidal function slowly tends to zero as the distance u increases (compared to other functions), and as

Table 5
Examples of most used autocorrelation functions.

Autocorrelation function	Autocorrelation length
$\rho_{ac}^{A} = \begin{cases} 1-\frac{\lvert u\rvert}{l_{ac}^{A}}; \lvert u\rvert \leqslant l_{ac}^{A} \\ 0 \quad ; \lvert u\rvert \leqslant l_{ac}^{A} \end{cases}$	$l_{ac}^{A} = l_{flu}$
$\rho_{ac}^{B}(u) = e^{-\left(\frac{u}{l_{ac}^{B}}\right)^2}$	$l_{ac}^{B} = \frac{1}{\sqrt{\pi}} l_{flu}$
$\rho_{ac}^{C} = \frac{\sin\left(\frac{u}{l_{ac}^{C}}\right)}{\frac{u}{l_{ac}^{C}}}$	$l_{ac}^{C} = \frac{1}{\pi} l_{flu}$

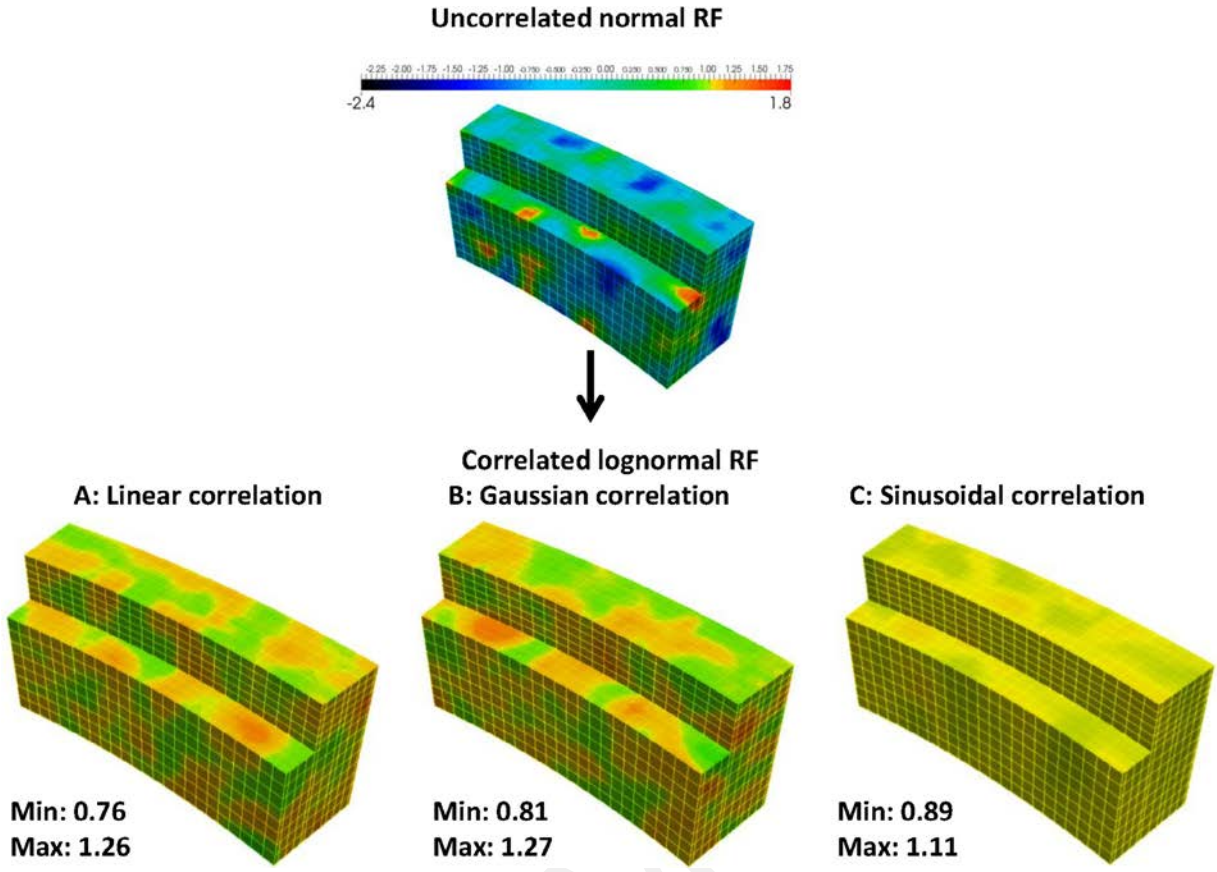

Fig. 10. Effect of the autocorrelation function on the spatial correlation of lognormal random fields.

shown in Fig. 10, less spatial scattering is obtained even though the autocorrelation distance is the least.[2] Accordingly, the model's response when using sinusoidal function should be closer to the one where no random fields (RF) are used.

In Table 4 the variation of each parameter is given along with the considered references.

For this step, the variables of interest are the peak strain at early-age, the number of cracks per 15° gusset RSV (Fig. 2c), the evolution of crack openings in time, the delayed strains due to creep and drying and their associated prestressing losses (linearly correlated to the crack openings during the operational phase as shown in Part I (Bouhjiti et al., 2018).

4.2. Pre-operational phase: Thermo-hydration and early-age cracking

4.2.1. Thermo-hydration calculation step

Given the numerical design plan in Table 2, the obtained results are shown in Fig. 11.

A global variation of 14% is obtained for the concrete's core temperature for the sensor G102 (variations from 12% to 16% are obtained for other positions). The most influential parameters are – as underlined in Briffaut et al. (2012) – : the hydration heat Q_∞ ($\delta^T_Q = 50\%, CoV^T_Q = 33\%, \overline{CoV^T_Q} = 82\%$), the thermal capacity C^p ($\delta^T_{C^p} = 40\%, CoV^T_{C^p} = 28\%, \overline{CoV^T_{C^p}} = 70\%$), and – as highlighted in Xian et al. (2014) – the heating process T_{heat} ($\delta^T_{T_{heat}} = 6\%, CoV^T_{T_{heat}} = 14\%, \overline{CoV^T_{T_{heat}}} = 35\%$) and the ambient temperature T_{ext} ($\delta^T_{T_{ext}} = 2\%, CoV^T_{T_{ext}} = 7\%, \overline{CoV^T_{T_{ext}}} = 14\%$).

[2] When the autocorrelation length is equal to zero, no spatial correlation is computed. When it tends to infinite value, the random field is reduced to a homogeneous field with a constant value.

The hydration and temperature effects on the concrete's thermal properties have, relatively, negligible effects on the concrete's peak temperature during hydration and have, accordingly, no influence on the mechanical behaviour at early age. This means that the expression $\lambda_c = (1.33-0.33\alpha)(1 + k_\lambda(T-T^{th}_{ref}))\lambda_{hc}(T^{th}_{ref})$ can be simplified into $\lambda_c = \lambda_{hc}(T^{th}_{ref})$ and $C^p_c = (1-k_{C^p}(T-T^{th}_{ref}))C^p_{hc}(T^{th}_{ref}) + (1-\alpha)k_{bw}\frac{c_0}{\rho_c}\zeta_\infty C^p_w$ into $C^p_c = C^p_{hc}(T^{th}_{ref})$. This result is opposed to conclusions in Briffaut et al. (2012) where such effects are not negligible (for a higher thermal gradient with a peak temperature of 60 °C) regarding thermal and mechanical aspects. In both studies the intrinsic variation of thermal parameters is demonstrated to be more important than the hydration effect or the temperature effect. However, in Briffaut et al. (2012) the identification of the source term Q_∞ in the heat equation has been performed using the hardened concrete properties which differs from what has been done in our study, where both hydration and temperature effects are considered during the identification and calculation phases. Consequently, the increase of concrete's thermal capacity is accompanied by an increase of the source term as well (for analytical developments one can refer to Appendix B in Bouhjiti et al., 2018) which eventually shows a compensatory effect lacked in Briffaut et al. (2012).

As for the hydration kinetic, the hydration heat is the main (if not only) influential parameter ($\delta^{Th}_Q = 98\%, CoV^{Th}_Q = 103\%, \overline{CoV^{Th}_Q} = 257\%$). An increase of its value leads to faster evolution of the hydration rate and therefore a faster increase of the concrete's mechanical properties.

Finally, three factors seem to be the most influential with regards to concrete thermo-hydration (and its mechanical behaviour afterwards):

- The chemical composition of the cement and cement content herein represented by the hydration heat Q_∞
- The thermal transfer properties of concrete herein referred to as the

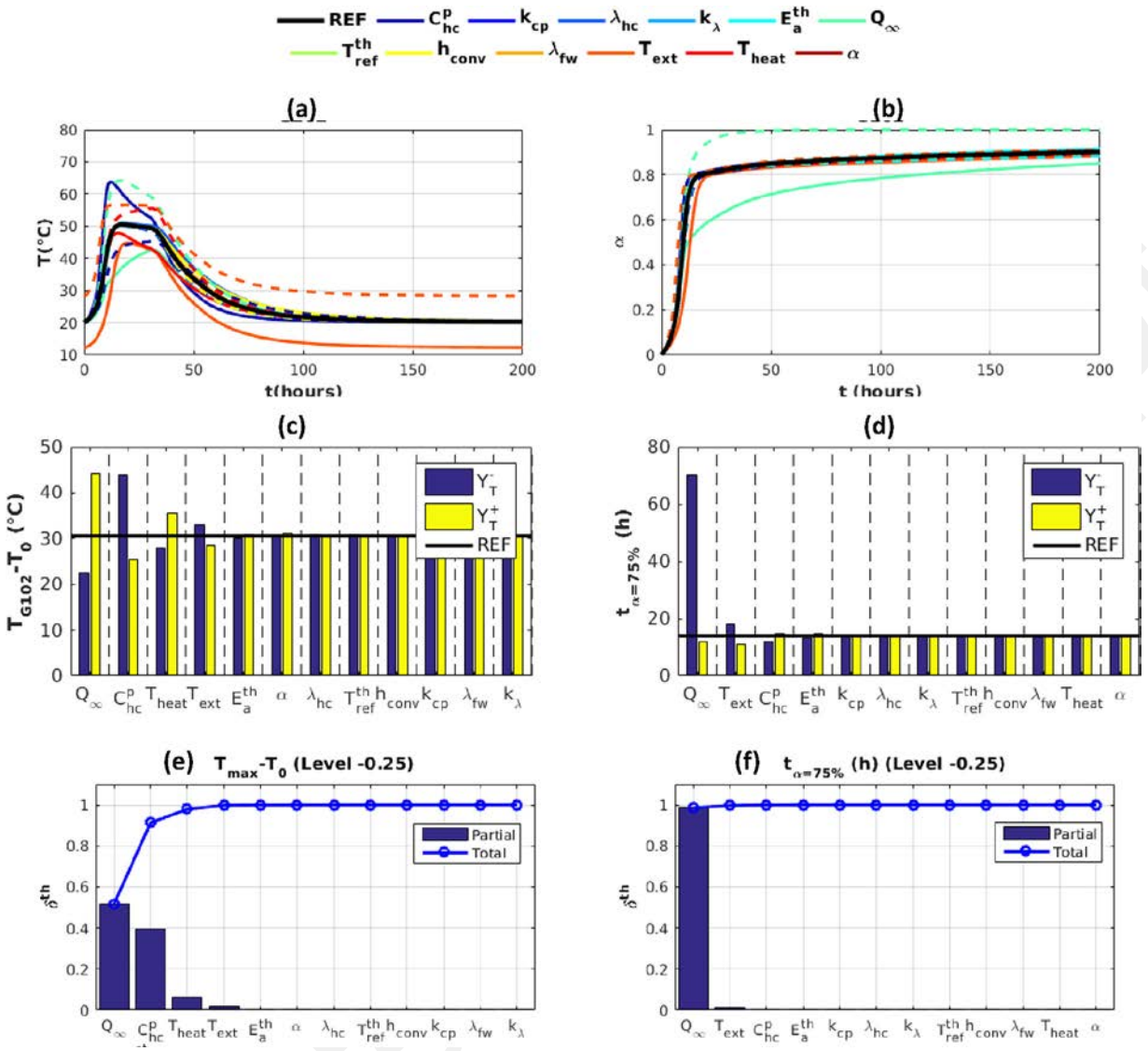

Fig. 11. 1st order sensitivity analysis of the VeRCoRs concrete's thermo-hydration (case of the G_{102} sensor): (a) Temperature profiles (b) Hydration rate evolution (c) Thermal gradient at the peak temperature (d) Time of hydration at 75% (e) Variance of thermal parameters with regards to maximal thermal gradient (f) Variance of thermal parameters with regards to the hydration rate.

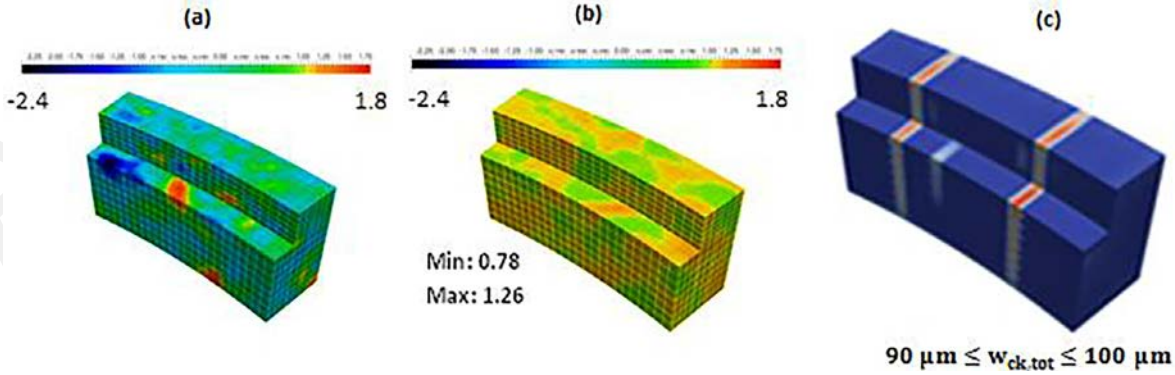

Fig. 12. Reference cracking pattern (2nd pattern in Bouhjiti et al., 2018 – Frequency 7/30) (a) Selected Gaussian RF (b) Resulting autocorrelated lognormal RF associated with the spatial scattering of the Young's modulus property (c) Reference cracking pattern with two cracks per 15° gusset RSV.

thermal capacity C_{hc}^{p}

– The curing conditions after casting (T_{heat} and T_{ext})

With that regard and within the considered domains of variation (Table 2), the effect of the remaining parameters is overlooked which allows the simplification of the heat equation in Eq. (6) into Eq. (10):

$$\text{During hydration: } \dot{T} - \frac{\lambda_{ch}}{\rho_c C_{hc}^{p}} \nabla \cdot (\nabla T) = \frac{Q_\infty}{\rho_c C_{hc}^{p}} \frac{d\alpha}{dt} e^{-\frac{E_a^{th}}{RT(t)}}$$
$$\text{After hydration: } \dot{T} - \frac{\lambda_{ch}}{\rho_c C_{hc}^{p}} \nabla \cdot (\nabla T) = 0 \quad (10)$$

with E_a^{th}, h_{conv}, λ_i, λ_{ch} parameters that can be identified with an error margin less than 40% without affecting the global thermal behaviour. C_{hc}^{p},λ_{ch},$\frac{d\alpha}{dt}$ identified without accounting for any hydration or temperature effects.

Moreover, by using Eq. (4), the CoV associated with the maximal thermal gradient ΔT_{max} can be defined. By inverse analysis (Eq. (11)) and given an observed variation of ΔT_{max} equal to 6% (Table 1), one can estimate the maximal onsite variation of each considered influential parameter: $CoV_{Q_\infty}^{max} = 8.5\%, CoV_{C^p}^{max} = 7\%, CoV_{T_{heat}}^{max} = 17\%$ which would induce the observed scattering of thermal behaviour on site (Fig. 4).

$$CoV^{\Delta T_{max}} \approx \sqrt{\left(0.82\,CoV_{Q_\infty}\right)^2 + \left(0.70\,CoV_{C^p}\right)^2 + \left(0.35\,CoV_{T_{heat}}\right)^2} \leqslant CoV^{\Delta T_{max,EXP}} = 0.06 \quad (11)$$

For the next calculation step (early age mechanical calculations), and to explore the effect of concrete's thermal behaviour on the early age cracking patterns, only two parameters are retained: the hydration

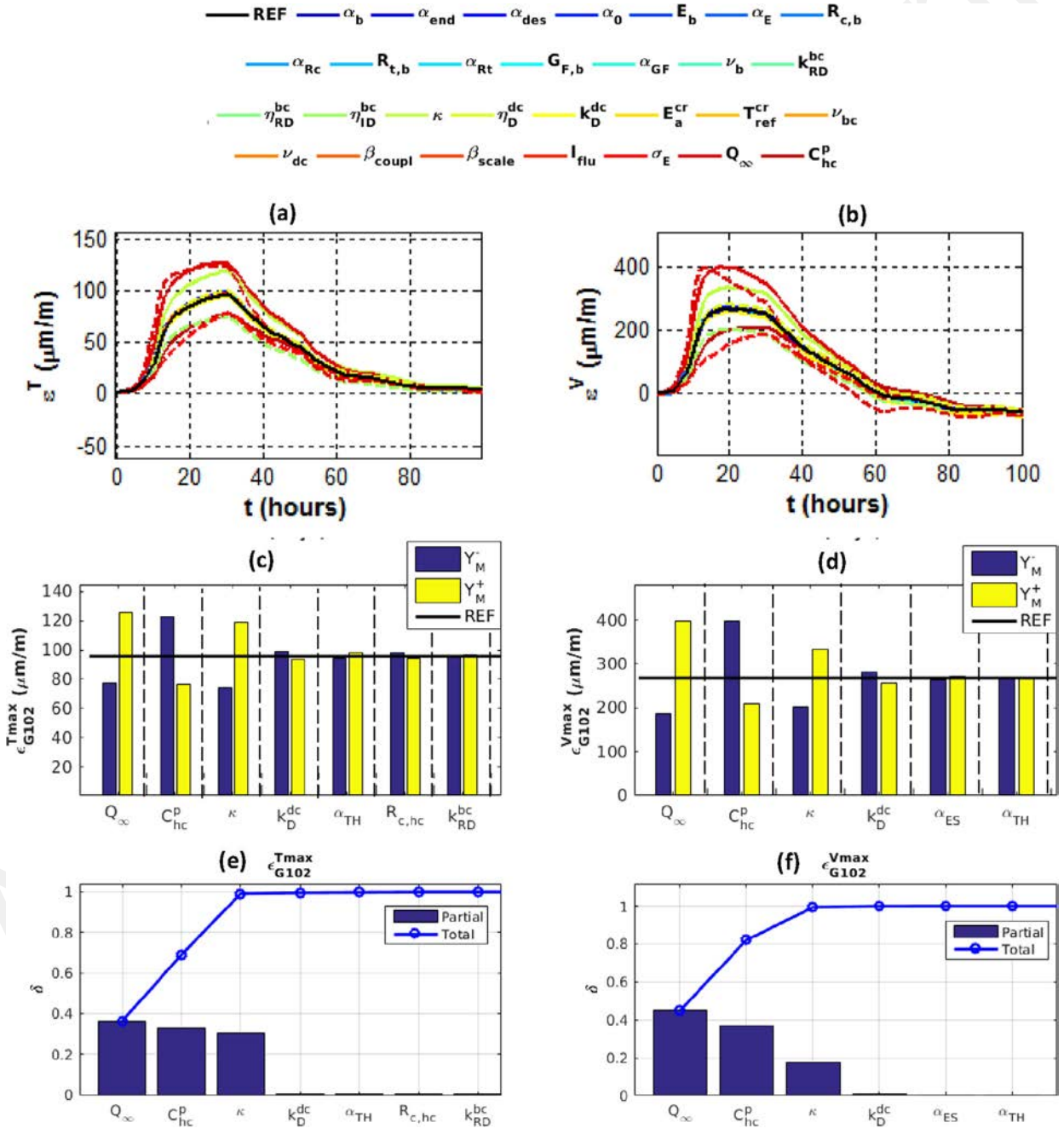

Fig. 13. 1st order sensitivity analysis of the VeRCoRs concrete's viscoelastic behaviour at early age (case of the G102 sensor): (a) Tangential strain profiles (b) Vertical strain profile (c) Tangential peak strain (d) Vertical peak strain (e) Variance of thermal and mechanical parameters with regards to the tangential peak strain (f) Variance of thermal and mechanical parameters with regards to the vertical peak strain.

heat Q_∞ and the thermal capacity C^p_{hc} with a cumulated variance of $\delta^T_Q + \delta^T_{C^p} = 90\%$. The definition of 90% as a cumulated variance threshold is indeed arbitrary aiming at limiting the required computational time for uncertainties propagation and still being able to explore the effects of the highest temperature variations on the following THM chains. Moreover, it is worth mentioning, that the heating at early age is not habitually performed for NCBs structural volumes. This has been the case for the VeRCoRs gusset in order to increase its thermal gradient and simulate the thermal behaviour of a full scale gusset.

4.2.2. Early-age cracking

As shown in Part I (Bouhjiti et al., 2018), the cracking patterns differ depending on the used RF realizations; accordingly one or two cracks are obtained per RSV (using 30 RF realizations). In order to limit the number of simulations and only evaluate the effect of the thermo-mechanical parameters, our sensitivity analysis (Table 4) is performed for a given RF realization (the selected one is the one for which two cracks are obtained per 15° RSV – Fig. 12). The obtained results are then generalized, at least from a qualitative point of view in the case of local responses, regardless of the used RF realizations. Indeed, from a quantitative point of view, the variation of the cracking pattern is inherently dependent on the used realization. In a second step, the spatial correlation effect is studied using the same inputs as in the reference analysis but different autocorrelation functions (Fig. 10).

4.2.2.1. Global mechanical response. For the peak strain during the hydration phase (Fig. 13), a global variation of 8% is obtained in the tangential direction (approximately same value for all sensors') and 11% in the vertical one (up to 16% for the lower extrados side). The most influential parameters are: the hydration heat Q_∞ (tangential: $\delta^M_Q = 36\%, CoV^M_Q = 24\%, \overline{CoV^M_Q} = 60\%$ – vertical: $\delta^M_Q = 45\%, CoV^M_Q = 37\%, \overline{CoV^M_Q} = 92\%$), the thermal capacity C^p (tangential: $\delta^M_{C^p} = 33\%, CoV^M_{C^p} = 23\%, \overline{CoV^M_{C^p}} = 57\%$ – vertical: $\delta^M_{C^p} = 37\%, CoV^M_{C^p} = 33\%, \overline{CoV^M_{C^p}} = 82\%$) and the creep ageing factor κ (tangential: $\delta^M_\kappa = 30\%, CoV^M_\kappa = 23\%, \overline{CoV^M_\kappa} = 115\%$ – vertical: $\delta^M_\kappa = 17\%, CoV^M_\kappa = 24\%, \overline{CoV^M_\kappa} = 120\%$). The rest of parameters have a negligible effect and, for the given variation domains, do not affect the concrete's global response at the structural scale in terms of strain evolution. Consequently, the mean strain scattering (local effects overlooked) is mainly due to the thermal behaviour variation at early age (in the absence of simultaneous drying). The result of κ, defined as a long term creep parameter, being an influential parameter at early age might appear surprising at first sight. However, when analysing the analytical 1D basic creep strain under a saturated environment and a constant load σ_0 (Eq. (12) derived from the Burgers model in Fig. 9 (Powers and Brownyard, 1946), the normalized coefficient of variation associated with κ is derived as shown in Eq. (13). It demonstrates that it has an effect on the observed strain as soon as concrete is subjected to stresses (which is the case when temperature rises during hydration) and not necessarily after the hydration ends.

$$\varepsilon_{1D}(t) = \frac{\sigma_0}{(1+\nu_{BC})k^{KV,dev}_{BC,0}}\left(1-e^{-\frac{k^{KV,dev}_{BC,0}}{\eta^{KV,dev}_{BC,0}}t}\right) + \frac{\kappa}{\sqrt{1+2\nu^2_{BC}}}\ln\left(\frac{\sigma_0\sqrt{1+2\nu^2_{BC}}}{\kappa(1+\nu_{BC})\eta^{M,dev}_{BC,0}}t+1\right) \quad (12)$$

$$\overline{CV^{\varepsilon_{1D}}_\kappa}(t) = \frac{1}{\sqrt{1+2\nu^2_{BC}}}\ln\left(\frac{\sigma_0\sqrt{1+2\nu^2_{BC}}}{\kappa(1+\nu_{BC})\eta^{M,dev}_{BC,0}}t+1\right) - \frac{\sigma_0 t}{\sigma_0\sqrt{1+2\nu^2_{BC}}\,t+\kappa(1+\nu_{BC})\eta^{M,dev}_{BC,0}} \quad (13)$$

Obviously, at the structural scale, the effect of κ is more difficult to predict analytically given the bidirectional and time dependent loading configuration. More importantly, the use of the Burgers model in its current version to describe early age creep is debatable since two ageing factors are included one explicitly associated with time and the other with the hydration rate to describe a priori the same physical phenomena. This aspect requires further experimental investigation and is considered out of the scope of the present study.

Eventually, three main parameters affect concrete strain during the hydration phase: the hydration heat Q_∞, the thermal capacity C^p and the Burgers model ageing factor κ with a cumulated variance $\delta^M_Q + \delta^M_{C^p} + \delta^M_\kappa = 99\%$ (only curves visible in Fig. 13a & b). Physically, they represent the thermal response and the maturity of concrete during the hydration phase. Based on those results, the viscoelastic response can be modelled with viscoelastic parameters identified within a 20% margin of error and the evolution of the Young's modulus at early age can be considered linearly related to the hydration rate. However, the ageing of viscoelastic properties should be identified with relatively higher precision (less than 20%).

The use of Eq. (4) and values from Table 1 leads to the definition of the associated CoV with the maximal strain components at early age (in the tangential ε^{max}_T and vertical ε^{max}_Vdirections – Eq. (14)). One can then estimate the maximal onsite variation of each considered influential parameter: From the thermo-hydration calculation step $CoV^{max}_{Q_\infty} = 8.5\%, CoV^{max}_{C^p} = 7\%$ leading, eventually, to $CoV^{max}_\kappa = 30\%$ (linearly extrapolated) which would induce the observed scattering of global mechanical behaviour on site (Fig. 5).

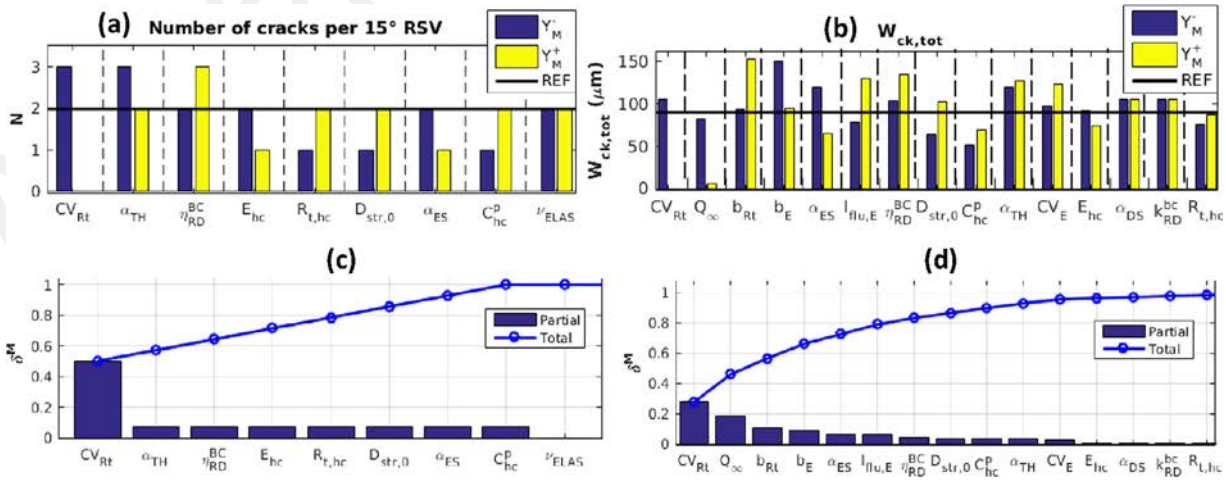

Fig. 14. 1st order sensitivity analysis of the VeRCoRs concrete's local behaviour at early age per 15° RSV: (a) Number of cracks (b) Total crack opening (c) Variance of thermal and mechanical parameters with regards to the number of cracks (d) Variance of thermal and mechanical parameters with regards to the total crack opening.

$$\mathrm{CoV}^{\varepsilon_T^{max}} \approx \sqrt{(0.60\mathrm{CoV}_{Q_\infty})^2 + (0.57\mathrm{CoV}_{C^p})^2 + (1.15\mathrm{CoV}_k)^2} \leqslant \mathrm{CoV}^{\varepsilon_T^{max,EXP}} = 0.34$$
$$\mathrm{CoV}^{\varepsilon_V^{max}} \approx \sqrt{(0.92\mathrm{CoV}_{Q_\infty})^2 + (0.82\mathrm{CoV}_{C^p})^2 + (1.20\mathrm{CoV}_k)^2} \leqslant \mathrm{CoV}^{\varepsilon_V^{max,EXP}} = 0.25 \quad (14)$$

4.2.2.2. Local mechanical response. When it comes to the local behaviour (cracking patterns in Fig. 14), the influential parameters differ from the previous ones and are in that sense more numerous; yet, descriptive of the known origins of cracking:

Size effect parameters: The tensile strength variation CoV_{R_t} in the used Statistical Size Effect Law (SSEL) seems to be the main influential input regarding the number of cracks ($\delta^M_{\mathrm{CoV}_{Rt}} = 50\%, \mathrm{CoV}^M_{\mathrm{CoV}_{Rt}} = 90\%, \overline{\mathrm{CoV}^M_{\mathrm{CoV}_{Rt}}} = 180\%$). This result was rather expected given the effect of CoV_{R_t} on the estimated Weibull modulus $m \approx 0.2 + \frac{1.2}{\mathrm{CoV}_{R_t}}$ and, accordingly, the reduction of the mean structural tensile strength in Eq. (8) compared to the rest of size effect parameters in Table 4. CoV_{R_t} is equally followed in terms of the induced variance ($\delta^M_{E_{hc}} = \delta^M_{R_t} = \delta^M_{D_{str,0}} = 07\%$) by two statistical size effect parameters (Eq. (8)) the Young's modulus E_{hc} ($\mathrm{CoV}^M_{E_{hc}} = 34\% - \overline{\mathrm{CoV}^M_{E_{hc}}} = 340\%$), the tensile strength $R_{t,hc}$ ($\mathrm{CoV}^M_{R_t} = 34\% - \overline{\mathrm{CoV}^M_{R_t}} = 340\%$) and another energetic size effect parameter $D_{str,0}$ the objective scale length ($\mathrm{CoV}^M_{D_{str,0}} = 34\% - \overline{\mathrm{CoV}^M_{D_{str,0}}} = 68\%$). The fluctuation length $l_{flu,E}$ used to perform spatial correlation and the Young's modulus coefficient of variation CoV_E do not seem to affect the number of cracks even with a 50% variation of their identified values.

Restraining effects: With the same variance ($\delta^M_{\alpha_{TH}} = \delta^M_{\alpha_{ES}} = \delta^M_{C^p} = \delta^M_{\eta^{KV,dev}_{BC}} = 07\%$), the following parameters also affect the modelled cracking response: the coefficient of thermal expansion CTE α_{TH} ($\mathrm{CoV}^M_{\alpha_{TH}} = 24\% - \overline{\mathrm{CoV}^M_{\alpha_{TH}}} = 240\%$), the endogenous shrinkage coefficient α_{ES} ($\mathrm{CoV}^M_{\alpha_{ES}} = 34\% - \overline{\mathrm{CoV}^M_{\alpha_{ES}}} = 340\%$), the thermal capacity C^p ($\mathrm{CoV}^M_{C^p} = 34\% - \overline{\mathrm{CoV}^M_{C^p}} = 85\%$) and the deviatoric Kelvin-Voigt chain viscosity $\eta^{KV,dev}_{BC,0} = \eta^{BC}_{RD}$[3] ($\mathrm{CoV}^M_{\eta^{KV,dev}_{BC}} = 24\% - \overline{\mathrm{CoV}^M_{\eta^{KV,dev}_{BC}}} = 120\%$).

It is important to underline again that, as far as the number of cracks is concerned, the obtained results cannot be generalized to all RF realizations in terms of resulting CoV or variance values. However, it is possible to conclude that the cracking patterns are at least affected by the parameters listed within the present sensitivity analysis. One can also notice how the effects of E_{hc},$R_{t,hc}$,$D_{str,0}$,α_{ES},C^p variation on the obtained cracking patterns are comparable to the one due the use of various RF realizations (1 or 2 cracks per 15° RSV). Nevertheless, the obtained frequencies of each cracking pattern are probably not the same as in the presented reference analysis (Bouhjiti et al., 2018). For instance, in the case of E_{hc} variation and for the same CoVc_E (Fig. 15b), the frequency of 1st cracking mode shifts from 50% to 20% (2nd mode from 50% to 5%) as E_{hc} is decreased by 10% (the remaining 70% are associated with mode 0 – no cracks –). And when it is increased by 10%, the frequency of the 1st cracking pattern becomes 25% (55% for the 2nd and 20% for 3rd i.e. 3 cracks per RSV). Eventually, this illustrates, the complexity of concrete's local behaviour modelling and the strong dependence of concrete cracking patterns' frequencies on both size effects (energetic: CoV_{R_t},$D_{str,0}$ and statistical: RF, E_{hc},$R_{t,hc}$), mechanical (α_{TH},α_{ES},$\eta^{KV,dev}_{BC,0}$) and thermal (C^p) properties. The absence of the hydration heat Q_∞ from this list simply means that the applied 40% variation is not enough to induce new cracking patterns. However, the risk of cracking remains indeed higher as the hydration heat increases but that does not mean the cracking mode would be different.

The observed cracking patterns on site are consequently the result of simultaneous intrinsic spatial variability of various mechanical parameters and random structural restraining effects. In order to still be able to perform an inverse analysis and describe the observed cracking patterns, one can either:

- Increase the number of RF realizations: this choice is hugely time consuming for large concrete structures modelling and is, given the actual calculation abilities, hard to achieve.
- Focus on one or two parameters variation for a given RF realization: in that sense, the role of RF is reduced to facilitating localization and introducing some heterogeneity which effect is higher than the deterministic one (due to the presence of steel and prestressing cables). The variation of the obtained cracking patterns would be due to the variation of the Young's modulus E_{hc} and/or tensile strength ($R_{t,hc}$,CoV_{R_t}) for instance. Such choice remains practical for engineering use even though it would probably require an overestimation of their CoV in order to compensate the constancy of other equally influential parameters. Our on-going work aims at investigating stochastic strategies with that regard.

As for crack openings at early age, their variations are depicted in Fig. 14 where the total crack openings are considered (cumulated over the total number of cracks). For the selected most influential parameters the total crack opening remains approximately the same and the opening per crack is linearly correlated to the number of cracks. For the rest of parameters, a maximum variation of 20 μm per crack is obtained over a mean opening of 50 μm even though the number of cracks remains the same.

4.2.2.3. Effect of spatial correlation. The computed cracking patterns can also be affected by the spatial correlation of the mechanical properties. In Fig. 15a, results are depicted for three different autocorrelation functions (Table 5) in addition to the case where no correlation is applied ($\rho_{ac} = 0$). One can notice in Fig. 15a that the same cracking modes are obtained (1 or 2 cracks per 15° RSV) for the used autocorrelation functions; what differs are the frequencies of each cracking pattern. Particularly, more cracks nearby the boundaries are obtained with the linear and sinusoidal functions which seem to favour the deterministic part of heterogeneity (due to the use of 1D rebars and prestressing cables) rather than the statistical size effect. For the sinusoidal function, this result is expected considering the reduced scattering of the autocorrelated RF (Fig. 10). When spatial correlation is not considered, the localization nearby the boundaries is the least and the frequency of the 2nd cracking pattern is higher. Even if such result remains in line with the one obtained using the Gaussian function (even better in terms of favouring statistical size effect), accounting for the spatial correlation is more representative of the mechanical parameters scattering especially if the fluctuation length is properly identified on site. The hypothesis of a null spatial correlation might lead to misrepresentative results in terms of cracking modes frequencies, though it doesn't seem to affect the identified cracking modes.

Ultimately, the following simplifications can be performed at early age given the insignificant effect of some parameters:

- The coupling factor between damage and creep does not seem to have an effect on the cracking patterns. For the obtained temporal thermal gradient, the developed tensile creep strains $\boldsymbol{\varepsilon^+_{CR}}$ remain negligible compared to the elastic component $\boldsymbol{\varepsilon^+_{ELAS}}$. For the VeRCoRs gusset, its value can therefore be fixed to 0.4 ± 0.2.
- For the considered prestressing loads, the basic creep Poisson ratio ν_{BC} can be considered equal to the elastic Poisson ratio ν_{ELAS} which would revoke the need for spherical and deviatoric decomposition of the used Burgers model: $\nu_{ELAS} = \nu_{BC}$.
- When interested in the number of cracks only, the mechanical parameters evolution with the hydration rate can be considered linear and the percolation threshold equal to zero: $X = \alpha X_{hc}$ where X is one of the mechanical properties (E,R_c,R_t,G_F), X_{hc} are the mechanical properties of hardened concrete.
- The fluctuation and objective scale lengths can be considered equal

[3] η^{BC}_{RD} stands for reversible deviatoric (RD) basic creep (BC) viscosity.

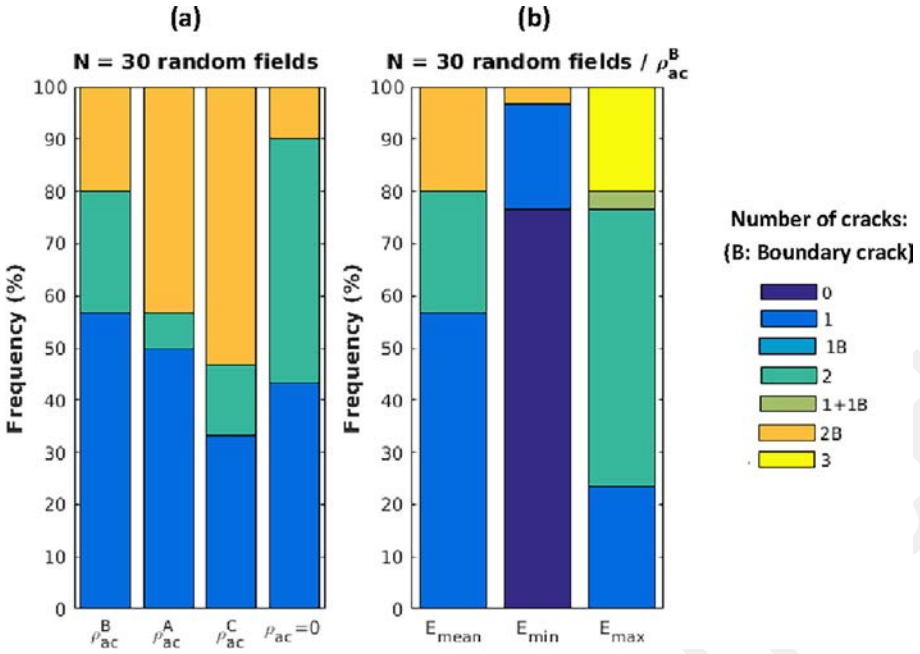

Fig. 15. (a) Autocorrelation effect and (b) Young's modulus variation effect on the 15° RSV cracking patterns.

and fixed at a conventional value of $l_{flu} = D_{str,0} = 1\,m$.

– For predictive calculations and in the absence of further information about concrete's mechanical properties' spatial variability, the default use of the Gaussian autocorrelation function seems reasonable to favour statistical size effects in comparison with deterministic heterogeneity effects (case of explicit modelling of rebars and prestressing cables).

4.3. Operational Phase: Drying and delayed cracking

4.3.1. Drying calculation step

Given the design plan in Table 3, the obtained results for the RH and saturation ratio S_r are shown in Fig. 16 (at the projected lifetime of VeRCoRs mock-up ~7 years).

A global variation of 7% is obtained for the concrete's core S_r and RH. As mentioned in Part I (Bouhjiti et al., 2018), the low RH at boundaries does not affect the global or mean water loss of the structure. This result is confirmed by our sensitivity analysis since a variation of 40% of the ambient RH has no effect on the concrete's bulk RH or S_r. The most influential parameters are: the initial water content $C_{w,0}$ (S_r: $\delta^W_{C_0} = 45\% - CoV^W_{C_0} = 17\% - \overline{\overline{CoV^W_{C_0}}} = 85\%$ - RH: $\delta^W_{C_0} = 34\% - CoV^W_{C_0} = 13\% - \overline{CoV^W_{C_0}} = 65\%$), the diffusivity parameter B_W (S_r: $\delta^W_{B_W} = 45\% - CoV^W_{B_W} = 17\% - \overline{CoV^W_{B_W}} = 85\%$ - RH: $\delta^W_{B_W} = 34\% - CoV^W_{B_W} = 13\% - \overline{\overline{CoV^W_{B_W}}} = 65\%$) and, in the case of RH, the desorption parameter $b_W (\delta^W_{b_W} = 19\% - CoV^W_{b_W} = 10\% - \overline{CoV^W_{b_W}} = 50\%)$. The two parameters $C_{w,0}$ and B_w are equally influential with regards to the saturation ratio given their positions in the drying equation Eq. (7). Indeed, if rewritten in terms of the saturation ratio instead of water content (Eq. (15)), Eq. (7) becomes :

$$\dot{S_r} = \nabla\cdot\left(A_w e^{C_{w,0}B_w S_r}\frac{T}{T^{dr}_{ref}}e^{-\frac{E^W_a}{R}\left(\frac{1}{T}-\frac{1}{T^W_{ref}}\right)}\nabla S_r\right) \tag{15}$$

It is reminded that the concrete is supposed initially saturated given the fact that a reduction of the initial water content induces also a reduction of the concrete's developed porosity during hydration (Brouwers, 2004; Brouwers, 2005; Zhu, 2014). As the available water for drying is less in a smaller porous domain, drying is harder to achieve which leads to higher saturation ratios and RH. The tendencies are inversed when the water content and the diffusivity factor are increased. As for the desorption parameter, and by definition, their influence becomes more important when solving the drying problem in terms of the RH instead of the saturation ratio. In all cases, their induced variance is considerably smaller compared to the one of $C_{w,0}$ and B_W which in total exceeds 70% for S_r and 90% for RH. Accordingly, these two parameters are retained for uncertainties propagation. Unfortunately, in the absence of experimental feedbacks, inverse analysis cannot be performed to define the parameters variation on site based on water content results (Eq. (2)). However, this can be achieved if the same parameters are retained as influential in the following THM step (long term mechanical calculations).

$$CoV^{S_r^\infty} \approx 0.85\sqrt{(CoV_{C_{w,0}})^2 + (CoV_{B_w})^2} \leqslant CoV^{S_r^\infty,EXP}$$
$$CoV^{RH^\infty} \approx 0.65\sqrt{(CoV_{C_{w,0}})^2 + (CoV_{B_w})^2 + 0.6\,(CoV_{b_w})^2} \leqslant CoV^{RH^\infty,EXP} \tag{16}$$

4.3.2. Ageing effect on cracking

The term ageing refers to drying and creep of concrete which induces prestressing losses and crack reopening during pressurization tests. With that regard, the variables of interest are:

The final strain at the end of the mock-up's projected lifetime due to creep and drying denoted $\boldsymbol{\varepsilon^{AG,\infty}}$ (Eq. (17))

$$\boldsymbol{\varepsilon^{AG,\infty}} = \boldsymbol{\varepsilon^{CR,\infty}} + \boldsymbol{\varepsilon^{DS,\infty}} \tag{17}$$

The prestressing losses represented by the continuously increasing residual tensile stresses in the tangential direction $\boldsymbol{\sigma_T^{RES}}$ during the pressurization phases. As demonstrated in Part I, and only where cracks have developed at early age, those stresses are linearly related to the crack openings by the means of a reduced Young's modulus (20% of the initial rigidity) in the tangential direction (Eq. (18)).

$$w_{ck} = < \frac{\sigma_T^{RES}}{0.2E_{hc}} >_+ \,[m] \tag{18}$$

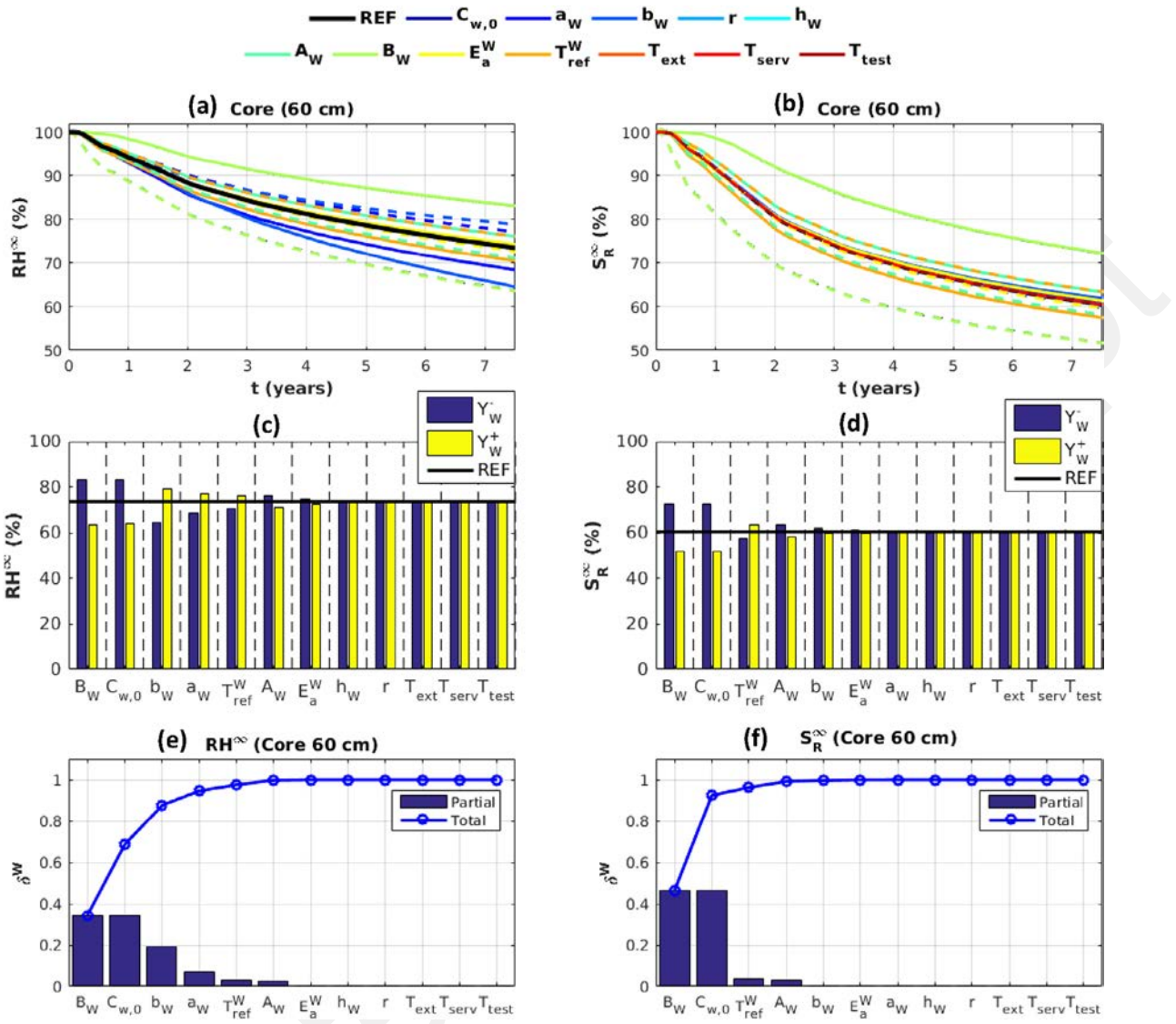

Fig. 16. 1st order sensitivity analysis of the VeRCoRs concrete's hydric behaviour (core of the gusset): (a) RH profiles (b) S_r profiles (c) RH at the projected lifetime (d) S_r at the projected lifetime (e) Variance of hydric parameters with regards to RH (f) Variance hydric parameters with regards to S_r.

To optimize the computational time, first calculations are performed within the viscoelastic framework to study the model's global response. Then, and once the most influential viscoelastic parameters during the operational phase are identified, calculations with damage are undertaken to evaluate how the cracking patterns evolve in time. Using values in Table 4, the obtained results are depicted in Figs. 17 and 18.

4.3.2.1. Viscoelastic analysis. For the ageing strain components (Fig. 17), the most influential parameters are: the initial water content $C_{W,0}$ (Vertical: $\delta_{C_0}^M = 34\% - \underline{CoV}_{C_0}^M = 19\% - \overline{CoV}_{C_0}^M = 95\%$- Tangential: $\delta_{C_0}^M = 63\% - \underline{CoV}_{C_0}^M = 34\% - \overline{CoV}_{C_0}^M = 170\%$), the drying shrinkage coefficient α_{DS} (Vertical: $\{\delta_{\alpha_{DS}}^M = 11\% - \underline{CoV}_{\alpha_{DS}}^M = 11\% - \overline{CoV}_{\alpha_{DS}}^M = 110\%$- Tangential: $\delta_{\alpha_{DS}}^M = 23\% - \underline{CoV}_{\alpha_{DS}}^{bfM} = 20\% - \overline{CoV}_{\alpha_{DS}}^M = 200\%$) and, in a less pronounced way, the diffusivity parameter B_W (Vertical: $\delta_{B_W}^M = 06\% - \underline{CoV}_{B_W}^M = 08\% - \overline{CoV}_{B_W}^M = 40\%$- Tangential: $\delta_{B_W}^M = 10\% - \underline{CoV}_{B_W}^M = 14\% - \overline{CoV}_{B_W}^M = 70\%$). In the vertical direction and given the importance of the effective prestressing loads compared to the ones in the tangential direction, the initial prestressing stress $\sigma_{ini}^{PREC}$is also influential $\delta_{\sigma_{ini}^{PREC}}^M = 45\% - \underline{CoV}_{\sigma_{ini}^{PREC}}^M = 22\% - \overline{CoV}_{\sigma_{ini}^{PREC}{}^M} = 44\%$ in terms of compressive loads reduction in time. These parameters have a cumulated variance of $\delta_{C_0}^M + \delta_{\alpha_{DS}}^M + \delta_{B_W}^M = 96\%$in the case of tangential ageing strain and $\delta_{\sigma_{ini}^{PREC}}^M + \delta_{C_0}^M + \delta_{\alpha_{DS}}^M = 90\%$ in the vertical one. So this list is more exhaustive than the one suggested in Berveiller et al. (2007a) where only drying parameters are retained. In particular, the initial prestressing loads and the drying shrinkage coefficient have a non-negligible effect on concrete's ageing. As for the rest of viscoelastic parameters, it seems that their identification within a 20% error's margin is enough to accurately describe the ageing of concrete. Moreover, the drying and basic creep Poisson ratios can be considered equal to the elastic Poisson ratio without affecting the computed global long term behaviour.

By inverse analysis, the coefficient of variation associated with the ageing strain $\varepsilon^{AG,\infty}$can therefore be written in line with Eq. (4) as following (Eq. (19)):

$$\begin{aligned} \mathrm{CoV}_{\varepsilon_T}^{AG,\infty} &\approx \sqrt{(1.70\mathrm{CoV}_{C_{w,0}})^2 + (2.00\mathrm{CoV}_{\alpha_{DS}})^2 + (0.70\mathrm{CoV}_{B_w})^2} \leqslant \\ &\mathrm{CoV}_{\varepsilon_T}^{AG,\infty,EXP} \\ \mathrm{CoV}^{\varepsilon_V^{AG,\infty}} &\approx \sqrt{(0.44\mathrm{CoV}_{\sigma_{ini}^{PREC}})^2 + (0.95\mathrm{CoV}_{C_{w,0}})^2 + (1.10\mathrm{CoV}_{\alpha_{DS}})^2} \leqslant \\ &\mathrm{CoV}^{\varepsilon_V^{AG,\infty,EXP}} \end{aligned} \tag{19}$$

As experimental measurements only cover the first 2 years of the

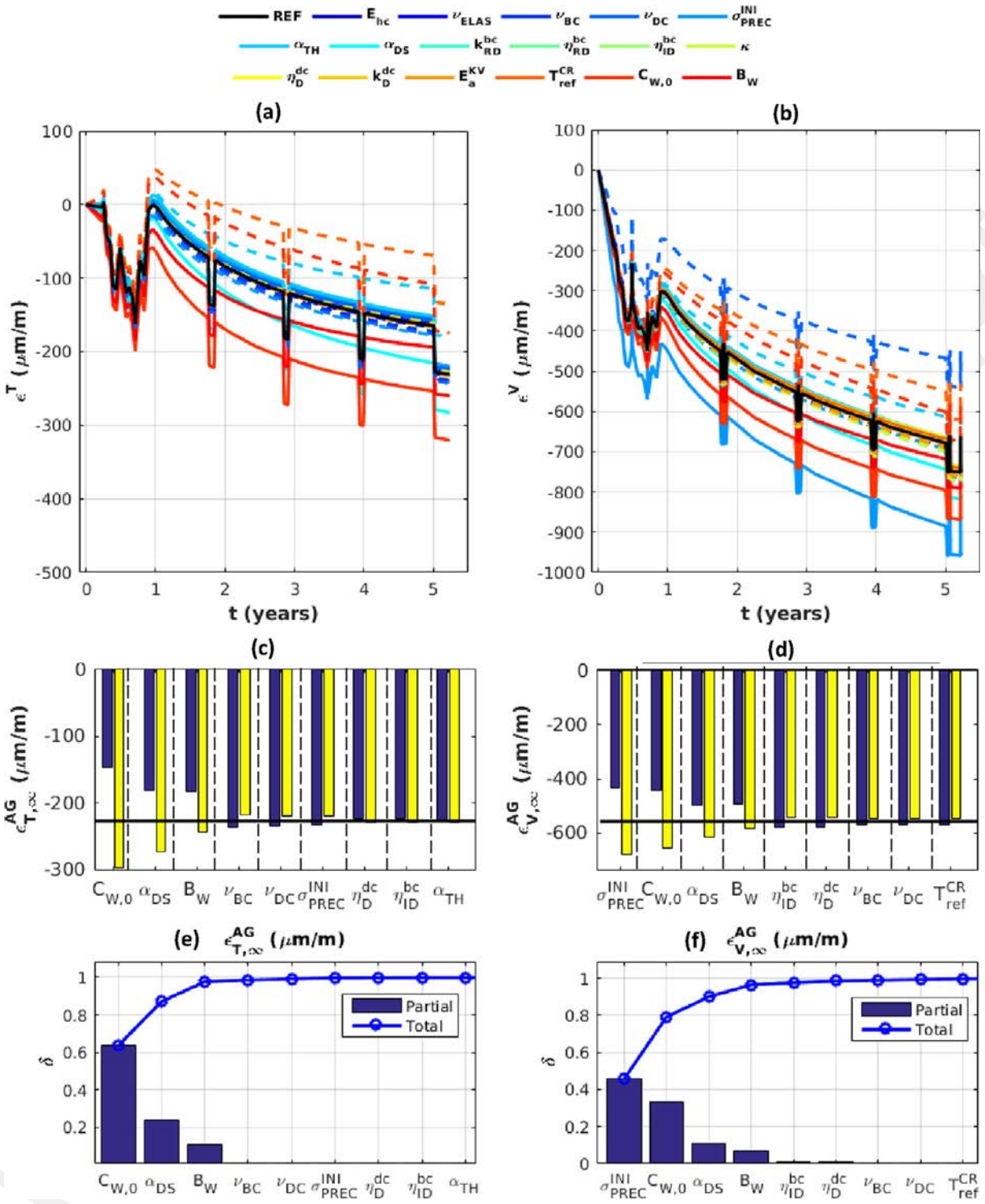

Fig. 17. 1st order sensitivity analysis of the VeRCoRs concrete's ageing behaviour (core of the gusset): (a) Tangential strain profiles (b) Vertical strain profiles (c) Tangential ageing strain at the projected lifetime (d) Vertical ageing strain at the projected lifetime (e) Variance of hydric and mechanical parameters with regards to tangential ageing strain (f) Variance of hydric and mechanical parameters with regards to vertical ageing strain.

VeRCoRs mock-up lifespan, the observed values for $CoV^{\epsilon^{AG,\infty,EXP}}$ are lacked. By using the observed variability so far ($CoV^{\epsilon^{AG,2yrs,EXP}}_{T} = 67\% - CoV^{\epsilon^{AG,2yrs,EXP}}_{V} = 38\%$), the obtained maximal variations are: $CoV^{max}_{C_{w,0}} = 40\%$, $CoV^{max}_{\alpha_{DS}} = 34\%$, $CoV^{max}_{\sigma^{PREC}_{ini}} = 86\%$ and $CoV^{max}_{B_w} = 95\%$. Clearly, the last value seems unrealistic which suggests that in the case of prestressing losses, contribution of both drying parameters ($C_{w,0}$,B_w) and mechanical loading (α_{DS},σ^{PREC}_{ini}) is needed to explain the observed on site variations (Fig. 6).

4.3.2.2. Damage-based analysis. It is underlined in part I (Bouhjiti et al., 2018) that, in the presence of early age cracks, the crack opening values are mainly controlled by the residual tensile stresses in the volume. Therefore, in Fig. 18 the residual stresses during pressurization tests (from 0 to 8) are plotted. As expected, the same influential parameters are obtained for the residual stresses and the ageing strains. In the

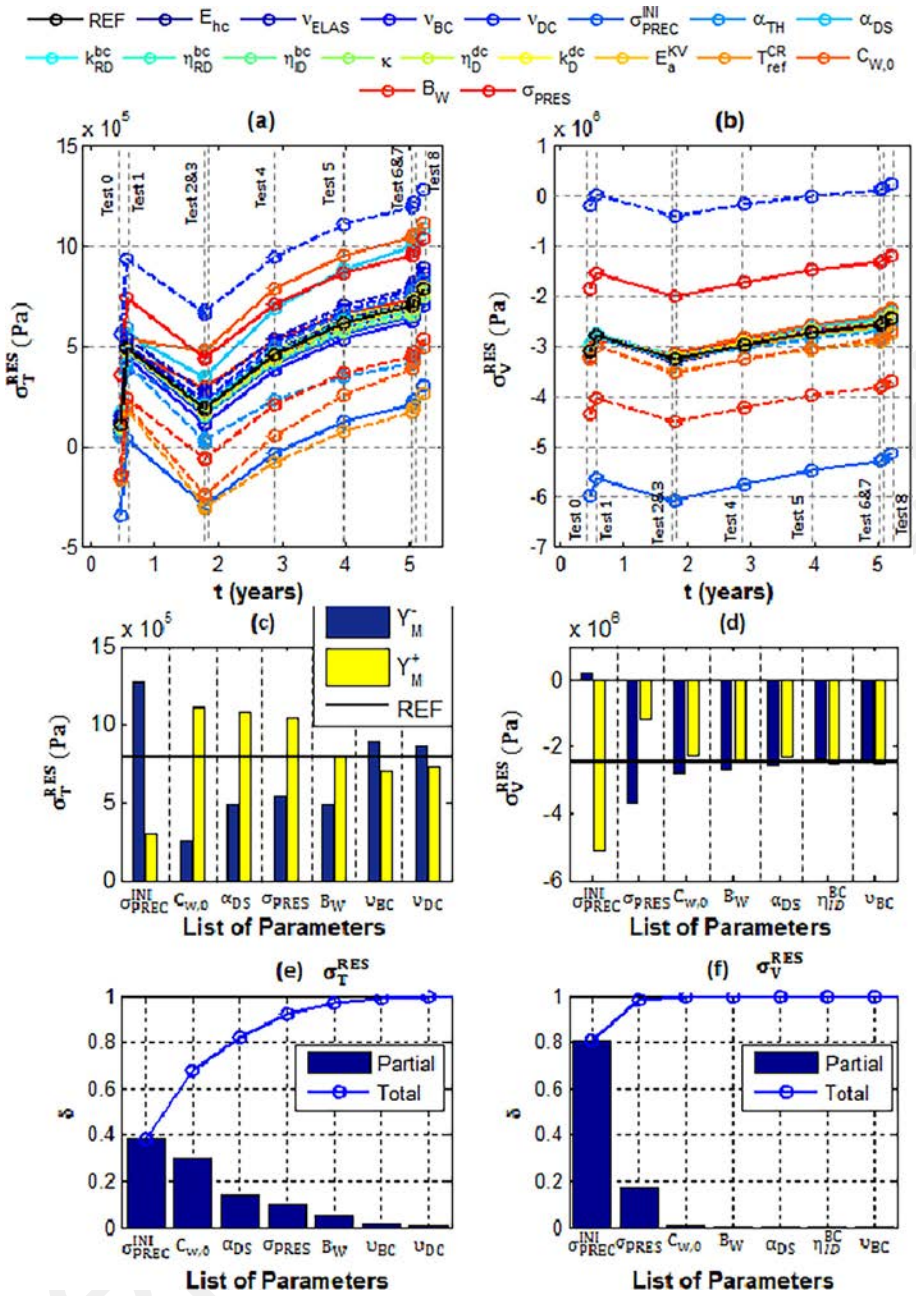

Fig. 18. 1st order sensitivity analysis of the VeRCoRs concrete's ageing effect on the residual stresses under pressurization loads ($\sigma_{RES} = \sigma_{PRES} + \sigma_{PREC}$): (a) Increase of the residual tensile stresses in the tangential direction due to prestressing losses (b) Increase of the residual tensile stresses in the vertical direction due to prestressing losses (c) Residual tangential stress during the pressurization test 8 (d) Residual vertical stress during the pressurization test 8 (e) Variance of hydric and mechanical parameters with regards to the residual tangential stress for test 8 (f) Variance of hydric and mechanical parameters with regards to the residual vertical stress for test 8.

tangential direction, however, the initial prestressing load appears as the most influential parameter which, depending on its value, ensures the existence of compressive stresses in concrete during the projected lifetime of the structure or, when being less effective, leads to a continuously increasing early age crack opening values (due to prestressing losses). In the vertical direction, two main parameters' seem to be influential: the prestressing and the applied pressurization loads. The obtained 1st order sensitivity indexes are the following: the initial prestressing load σ^{PREC}_{ini} (Tangential: $\delta^{M}_{\sigma^{PREC}_{ini}} = 38\% - CoV^{M}_{\sigma^{PREC}_{ini}} = 62\% - \overline{CoV^{M}_{\sigma^{PREC}_{ini}}} = 124\% -$ Vertical: $\delta^{M}_{\sigma^{PREC}_{ini}} = 81\% - CoV^{M}_{\sigma^{PREC}_{ini}} = 109\% - \overline{CoV^{M}_{\sigma^{PREC}_{ini}}} = 218\%$), the initial water content $C_{w,0}$ (Tangential: $\delta^{M}_{C_{w,0}} = 30\% - CoV^{M}_{C_{w,0}} = 59\% - \overline{CoV^{M}_{C_{w,0}}} = 295\%$), the drying shrinkage coefficient (Tangential: $\delta^{M}_{\alpha_{DS}} = 14\% - CoV^{M}_{\alpha_{DS}} = 36\% - \overline{CoV^{M}_{\alpha_{DS}}} = 360\%$), the applied pressurization load (Tangential: $\delta^{M}_{\sigma_{PRES}} = 10\% - CoV^{M}_{\sigma_{PRES}} = 32\% - \overline{CoV^{M}_{\sigma_{PRES}}} = 64\% -$ Vertical: $\delta^{M}_{\sigma_{PRES}} = 17\% - CoV^{M}_{\sigma_{PRES}} = 51\% - \overline{CoV^{M}_{\sigma_{PRES}}} = 102\%$), the drying parameter B_W (Tangential: $\delta^{M}_{B_W} = 05\% - CoV^{M}_{B_W} = 26\% - \overline{CoV^{M}_{B_W}} = 130\%$). The creep Poisson ratios (ν_{BC} and ν_{DC}) show slight influence with regards to the residual stresses but not as much as the previous parameters.

One can notice that, in the vertical direction, and within the considered domains of variation, concrete remains under compressive loads. So the chances of developing horizontal cracks during pressurization tests are negligible. On the contrary, in the tangential direction, residual stresses are mainly positive (tensile loads). In the absence of early age cracks, and based on the numerically computed residual

stresses, crack initiation is hard to achieve (residual stresses inferior to the tensile strength of concrete ~2.9 MPa). However, in the presence of early age cracks, their reopening is certain. Based on damage-based simulations (performed for $\min(\sigma_{\text{ini},T}^{\text{PREC}}) = 0.25MPa$ and $\max(\sigma_{\text{ini},T}^{\text{PREC}}) = 0.75MPa$), the number of cracks obtained at early age (in the reference analysis – Fig. 12), does not evolve in time as the concrete ages. This result is rather expected given the order of the tensile residual stresses (not enough to induce new cracks). Also, Eq. (18) remains locally (and numerically) verified to describe crack openings using a reduced structure's rigidity in the tangential direction (80% reduction). This validates the decoupling of damage-based early age calculations and long term viscoelastic ageing simulations – recommended in part I (Bouhjiti et al., 2018) for computational time optimization – with respect to Eq. (18). For prestressed concrete structures, particularly NCBs, the early age calculations should only be interested in the number of cracks whereas the viscoelastic analysis covering concrete creep and drying shrinkages should focus on the prestressing losses as the applied prestressing loads do not allow the development of new cracks. The combination of the two leads to the definition of the crack opening values during the pressurization tests and their evolution in time.

Eventually, the parameters affecting crack opening values during pressurization are the same as the ones affecting the tangential residual stresses: the initial prestressing load $\sigma_{\text{ini}}^{\text{PREC}}$ (Tangential: $\delta_{\sigma_{\text{ini}}^{\text{PREC}}}^{M} = 38\% - CoV_{\sigma_{\text{ini}}^{\text{PREC}}}^{M} = 62\% - \overline{CoV}_{\sigma_{\text{ini}}^{\text{PREC}}}^{M} = 124\%$), the initial water content $C_{w,0}$ (Tangential: $\delta_{C_{w,0}}^{M} = 30\% - CoV_{C_{w,0}}^{M} = 59\% - \overline{CoV}_{C_{w,0}}^{M} = 295\%$), the drying shrinkage coefficient (Tangential: $\delta_{\alpha_{DS}}^{M} = 14\% - CoV_{\alpha_{DS}}^{M} = 36\% - \overline{CoV}_{\alpha_{DS}}^{M} = 360\%$), the applied pressurization load (Tangential: $\delta_{\sigma_{\text{PRES}}}^{M} = 10\% - CoV_{\sigma_{\text{PRES}}}^{M} = 32\% - \overline{CoV}_{\sigma_{\text{PRES}}}^{M} = 64\%$) and finally the drying parameter B_W (Tangential: $\delta_{B_W}^{M} = 05\% - CoV_{B_W}^{M} = 26\% - \overline{CoV}_{B_W}^{M} = 130\%$). And the variation associated with tangential crack opening values writes:

$$CoV^{w_{ck}} \approx \sqrt{\begin{aligned}&\left(1.24CoV_{\sigma_{\text{ini},T}^{\text{PREC}}}\right)^2 + \left(2.95CoV_{C_{w,0}}\right)^2 + \left(3.60CoV_{\alpha_{DS}}\right)^2 \\ &+ \left(0.64CoV_{\sigma_{\text{PRES}}}\right)^2 + \left(1.30CoV_{B_W}\right)^2\end{aligned}} \tag{20}$$

5. Conclusions

This contribution presented a 1st order sensitivity analysis of the suggested THM model in part I. Applied to more than 50 inputs at the scale of the VeRCoRs gusset's RSV, the OFAT method allowed the identification of a reduced list of the most influential parameters affecting the concrete's early age and delayed behaviours. Moreover, and by inverse analysis, the CoV of those various inputs have been approximated based on available in situ measurements. Within the used variation domains and based on the obtained results at the scale of the VeRCoRs gusset RSV scale, the following conclusions are retained:

- About the THM modelling strategy and POP/OP decoupling
  - The thermo-hydration calculations can be performed without accounting for the thermal and hydration effects on the concrete's thermal properties.
  - The drying calculations can be performed using desorption curve only without distinguishing the sorption and desorption curves.
  - The use of the Burgers model to describe basic and drying creep can be performed without distinguishing the deviatoric and spherical parts (creep Poisson ratios equal to the elastic one).
  - The evolution of the mechanical properties at early age can be linearly related to the hydration rate.
  - The fluctuation and objective scale lengths needed to define statistical and energetic size effects respectively can be considered equal and fixed at a conventional value of $l_{\text{flu}} = D_{\text{str},0} = 1\text{m}$ for large concrete structures.
  - As the number of cracks remains the same as the one identified at early age during the whole gusset's lifetime, the behaviour of concrete during the operational phase can be performed using viscoelastic approaches. The crack opening estimation (locally where early age cracks have developed) can be performed using the ratio of the residual tensile tangential stresses to a reduced value of the Young's modulus (80% reduction herein).
- About the most influential parameters at early age
  - The thermal behaviour of concrete at early age is mainly affected by the hydration heat $Q_\infty$and the thermal capacity C^p variations. Even though, the ambient temperature considerably affects concrete peak temperature, it does not affect as much its thermal gradient (over time) which is associated with thermal shrinkage and crack development. By inverse analysis based on VeRCoRs in situ measurements, those two parameters show a variation of 8% on site. An error's margin of 40% can be retained for the rest of thermal properties without affecting the model's response (in terms of temporal thermal gradient).
  - The cracking patterns are affected as much by the suggested SSEL and RF parameters as by the concrete's mechanical and viscoelastic properties (such as the thermal and endogenous shrinkages or ageing parameters in the Burgers model). In situ cracking patterns can be practically found by inverse analysis through the variation of many parameters. For the sake of practicality, and as the use of numerous RF realizations leads to heavy computational time, the tensile strength and the Young's modulus can be used for such purpose. However, this choice cannot be retained for predictive calculations unless their variations account for the uncertainties associated with the rest of equally influential inputs. For the VeRCoRs concrete, the intrinsic variation of the tensile strength is limited to 10%. However, a 25% variation is required to identify numerically all the cracking patterns observed on site. Our on-going work is geared towards the definition of a SSEL-based stochastic approach to associate probabilities of occurrence to the predicted cracking patterns. In that sense, the default choice of the Gaussian autocorrelation function is retained and the RF role is diminished to facilitating localization and introducing enough heterogeneity to overcome deterministic heterogeneity effects due to the explicit modelling of rebars.
- About the most influential parameters on concrete's ageing
  - Drying behaviour is mainly driven by the concrete mix design in terms of the initial water content $C_{W,0}$and the water particles diffusion through the porous media ($B_w$parameter). The two are equally influential on the relative humidity RH and the saturation ratio S_r. The rest of the hydric parameters can be identified with an error's margin of 20% and the applied hydric flux with a precision of 40% without affecting the concrete's mean hydric behaviour.
  - The main phenomenon affecting concrete creep and prestressing losses is drying. Accordingly, the initial water content $C_{W,0}$ and the drying shrinkage coefficient $\alpha_{DS}$are the most influential parameters. By inverse analysis, their variation on site for VeRCoRs mock-up would be around 40%. However, in terms of early age crack reopening risk, most influential parameters, in addition to the previous ones, are related to the gusset's RSV mechanical boundary conditions; especially, the restraining effects during the prestressing and pressurization phases. In the case of the VeRCoRs gusset, they show high scattering (more than 50% variation on site) and represent 50% of the induced variance associated with the residual tensile stresses in concrete (they have the same influence on the crack opening values). Those structural effects remain unknown a priori and strongly depend on the quality/properties of casting joints. Consequently, the characterization of concrete behaviour in this region is worth exploring. The coefficient of drying shrinkage α_{DS}seems also to have a non-negligible effect on the computed residual tensile stresses. As for the viscoelastic properties of concrete, an error's margin of 20% can be tolerated at identification without affecting concrete creep at the structural scale.

– As uncertainties are propagated, the effect of drying on the computed local mechanical behaviour is demonstrated to be higher than the one on the global mechanical behaviour or the global hydric response. This aspect is illustrative of uncertainties amplification throughout the THM chain and shows the importance of uncertainties propagation when concrete cracking is of interest.

Finally, with regards to concrete cracking, from more than 50 parameters, only 9 inputs have been retained and judged as most influential : (Q_∞,C^p,E,R_t) at early age and for the long term behaviour ($C_{w,0}$,B_w,α_{DS},σ^{ini}_{PREC},σ_{PRES}). This should facilitate higher order sensitivity analyses and serve as a basis for future probabilistic descriptions of concrete cracking and ageing.

Acknowledgments

This work was supported by EDF-SEPTEN/DTG/CIH within the Chair PERENITI agreement with the Grenoble INP Partnership Foundation. The author is grateful to EDF-SEPTEN for the provided in situ measurements and to EDF R&D for the granted access to EDF's numerical cluster. The author is thankful to Assoc. Prof. BRIFFAUT Matthieu for his interest in this work and the stimulating discussions he contributed to. The Chair PERENITI partners shall not in any circumstances be deemed liable for the content of this publication which is only binding its author. The 3SR lab is part of the LabEx Tec 21 (Investissements d'Avenir - Grant agreement n°ANR-11-LABX-0030).

References

Ditlevsen, O., Madsen, H.O., 1996. Structural Reliability Methods. Wiley ISBN: 0471960861, 9780471960867.

Baroth, J., Breysse, D., Schoefs, F., 2011. Construction Reliability: Safety, Variability and Sustainability. Wiley-ISTE ISBN: 978-1-84821-230-5.

Bouhjiti, D.E.-M., Baroth, J., Briffaut, M., Dufour, F., Masson, B., 2018. Statistical modeling of cracking in large concrete structures under thermo-hydro-mechanical loads: application to nuclear containment buildings. Part 1: random field effects (reference analysis). Nucl. Eng. Des. 333, 196–223. http://dx.doi.org/10.1016/j.nucengdes.2018.04.005.

Briffaut, M., Benboudjema, F., Torrenti, J.M., Nahas, G., 2012. Effects of early age thermal behaviour on damage risks in massive concrete structures. Eur. J. Civ. Environ. Eng. 16 (5), 589–605. http://dx.doi.org/10.1080/19648189.2012.668016.

Xian, L., Yong, Y., Quanke, S., 2014. Sensitivity analysis of the early-age cracking risk in immersed tunnel. Struct. Concr. 15 (2), 179–190. http://dx.doi.org/10.1002/suco.201300064.

Defraeye, T., Blocken, B., Carmeliet, J., 2013. Influence of uncertainty in heat–moisture transport properties on convective drying of porous materials by numerical modelling. Chem. Eng. Res. Des. 91 (1), 36–42. http://dx.doi.org/10.1016/j.cherd.2012.06.011.

Trabelsi, A., Hamami, A., Belarbi, R., Turcry, P., Aït-Mokhtar, A., 2012. Assessment of the variability of moisture transfer properties of High Performance Concrete from a multi-stage drying experiment. Eur. J. Environ. Civ. Eng. 16 (3–4), 352–361. http://dx.doi.org/10.1080/19648189.2012.667713.

de Larrard, T., Colliat, J.B., Benboudjema, F., Torrenti, J.M., Nahas, G., 2010. Effect of the young modulus variability on the mechanical behaviour of a nuclear containment vessel. Nucl. Eng. Des. 240 (12), 4051–4060. http://dx.doi.org/10.1016/j.nucengdes.2010.09.031.

Briffaut, M., Benboudjema, F., Torrenti, J.-M., Nahas, G., 2011. Numerical analysis of the thermal active restrained shrinkage ring test to study the early age behavior of massive concrete structures. Eng. Struct. 33 (4), 1390–1401. http://dx.doi.org/10.1016/j.engstruct.2010.12.044.

Berveiller M., Le Pape Y., Sudret B. Sensitivity analysis of the drying model on the delayed strain of concrete in containment vessels with a non intrusive method. ICASP10 Proceedings 2007 Tokyo Japan.

Berveiller M., Le Pape Y., Sudret B., Perrin F. Bayesian updating of the long-term creep strains in concrete containment vessels using a non intrusive stochastic finite element method. ICASP10 Proceedings 2007 Tokyo Japan.

A. Saltelli, M. Ratto, T. Andres, F. Campolongo, J. Cariboni, D. Gatelli, M. Saisana, S. Tarantola. Global Sensitivity Analysis: The Primer. Wiley/Mathematics & Statistics/Applied probability & Statistics/Models 2018 Chapter II: 53–108.

Corbin M., Garcia M. Benchmark VERCORS report 2015 (https://www.conference-service.com/EDF-VeRCoRs-Benchmark-2018/welcome.cgi).

Sobol' I.M, 2001. Global sensitivity indices for nonlinear mathematical models and their Monte Carlo estimates. Mathematica and computers in simulation. 55(1–3):271–280. doi:10.1016/S0378-4754(00)00270-6.

Cotter, S.C., 1979. A screening design for factorial experiments with interactions. Biometrika 66 (2), 317–320. http://dx.doi.org/10.1093/biomet/66.2.317.

COMMISSION 42-CEA, 1981. Properties of set concrete at early ages (State of the art report). Mater. Struct. 14 (16), 399–401. http://dx.doi.org/10.1007/BF02476348.

Neville, A.M., 2004. Properties of Concrete, fourth ed. Pearson Education.

Taylor, H.F.W., 1997. Cement Chemistry. Thomas Telford, London UK.

Waller. V. Relation entre formulation d'un béton et propriétés mécaniques, formulation et chaleur d'hydratation, cas de cendres volantes. PhD thesis 1991 ENPC. Paris, France.

Schindler, K., Folliard, J., 2005. Heat hydration models for cementitious materials. ACI Mater. J. 102 (1), 24–33.

Powers, T.C., Brownyard, T.L., 1946. Studies of the physical properties of hardened Portland cement of paste. ACI Proceedings 43 (9), 469–504.

Mills R.H, 1966. Factors influencing cessation of hydration in water cured cement pastes. HRB SR 90 (Washington. USA) 406–424.

Issadi N., Hamami A.E.A., Belarbi R., Ait-Mokhtar A, 2016. Incidence de la variabilité spatiale de quelques propriétés de transfert du béton sur son comportement hygro-thermique. JFMS'16 Nancy, France.

Granger L, 1995. Comportement différé du béton dans les enceintes de centrales nucléaires. PhD thesis ENPC [in French]. France.

Mazars, J., Hamon, F., Grange, S., 2015. A new 3D damage model for concrete under monotonic, cyclic and dynamic loadings. Mater. Struct. 48 (11), 3779–3793. http://dx.doi.org/10.1617/s11527-014-0439-8.

De Schutter, G., Taerwe, L., 1996. Degree of hydration-based description of mechanical properties of early age concrete. Mater. Struct. 29 (6), 335–344. http://dx.doi.org/10.1007/BF02486341.

Torrenti J.M., Benboudjema F, 2005. Comportement au jeune âge du béton: approche 3D du seuil de percolation mécanique. 23ème rencontres universitaires de GC – risque et environnement France.

Charpin, L., Le Pape, Y., Masson, B., 2015. EDF study of 10-years concrete creep under unidirectional and biaxial loading: evolution of poisson coefficient under sealed and unsealed conditions. Proceedings CONCREEP 10, 1381–1390.

Berveiller M., Le Pape Y., Sudret B., Perrin F., 2007. Bayesian updating of long –term creep strains in concrete containment vessels using a non-intrusive stochastic finite element method. In: Int. Conf. Applications of statistics and Probability in Civil Engineering, ICASP'10 Tokyo, Japan.

Berveiller, M., Le Pape, Y., Bruno, S., 2012. Updating the long-term creep strains in concrete containment vessels by using Markov chain Monte Carlo simulation and polynomial chaos expansions. Struct. Infrastruct. Eng. 8 (5), 425–440. http://dx.doi.org/10.1080/15732479.2010.539057.

De Larrard T., 2010. Variabilité des propriétés du béton : caractérisation expérimentale et modélisation probabiliste de la lixiviation. PhD ENS Cacha [in French]. France.

Sellier, A., Millard, A., 2014. Weakest link and localization WL^2: a method to conciliate probabilistic and energetic scale effects in numerical models. Eur. J. Environ. Civ. Eng. 18 (10), 1177–1191. http://dx.doi.org/10.1080/19648189.2014.906368.

Ghannoum, M., Baroth, J., Rospars, C., Millard, A., 2017. Prediction of the size effect in concrete structures using ana analytical approach to the weakest link and localization method (WL2). Mater. Struct. http://dx.doi.org/10.1617/s11527-017-1049-z.

Foucault, A., Michel-Ponnelle, S., Galenne, E., 2012. A new creep model for NPP containment behaviour prediction. International conference on Numerical modelling Strategies for sustainable concrete structures.

Powers, T.C., Brownyard, T.L., 1946. Studies of the physical properties of hardened Portland cement of paste. ACI Proceedings 43 (9), 469–504.

Brouwers, H.J.H., 2004. The work of Powers and Brownyard revisited: Part 1. Cem. Concr. Res. 34 (9), 1697–1716. http://dx.doi.org/10.1016/j.cemconres.2004.05.031.

Brouwers, H.J.H., 2005. The work of Powers and Brownyard revisited: Part 2. Cem. Concr. Res. 35 (9), 1922–1936. http://dx.doi.org/10.1016/j.cemconres.2005.04.009.

Zhu, B., 2014. Thermal stresses and temperature control of mass concrete. China Institute of Water Resources and Hydropower Research and Chinese Academy of Engineering Ed Elsevier.